F. Bariselli, A. Frezzotti, A. Hubin, T.E. Magin
Aerothermodynamic Modelling of Meteor Entry Flows
Monthly Notices of the Royal Astronomical Society, Vol. 492, N. 2, 2020, p. 2308-2325
doi:10.1093/mnras/stz3559

Monthly Notices
of the
ROYAL ASTRONOMICAL SOCIETY

MNRAS **492,** 2308–2325 (2020)
Advance Access publication 2019 December 19

doi:10.1093/mnras/stz3559

Aerothermodynamic modelling of meteor entry flows

Federico Bariselli ,[1,2,3]★ Aldo Frezzotti,[3] Annick Hubin[1] and Thierry E. Magin[2]

[1]*Research Group Electrochemical and Surface Engineering, Vrije Universiteit Brussel, Pleinlaan 2, B-1050 Brussel, Belgium*
[2]*Aeronautics and Aerospace Dept., von Karman Institute for Fluid Dynamics, Waterloosestwg. 72, B-1640 St.-Genesius-Rode, Belgium*
[3]*Dipartimento di Scienze e Tecnologie Aerospaziali, Politecnico di Milano, Via La Masa 34, I-20156 Milano, Italy*

Accepted 2019 December 16. Received 2019 November 29; in original form 2019 July 27

ABSTRACT

Due to their small size and tremendous speeds, meteoroids often burn up at high altitudes above 80 km, where the atmosphere is rarefied. Ground radio stations allow us to detect the concentration of electrons in the meteoroid trail, which are produced by hyperthermal collisions of ablated species with the freestream. The interpretation of these data currently relies on phenomenological methods, derived under the assumption of free molecular flow, that poorly accounts for the detailed chemistry, diffusion in the vapour phase, and rarefied gas effects. In this work, we employ the direct simulation Monte Carlo (DSMC) method to analyse the detailed flowfield structure in the surroundings of a 1 mm meteoroid at different conditions, spanning a broad spectrum of Knudsen and Mach numbers, and we extract resulting ionization efficiencies. For this purpose, we couple the DSMC method with a kinetic boundary condition which models evaporation and condensation processes in a silicate material. Transport properties of the ablated vapour are computed following the Chapman–Enskog theory starting from Lennard–Jones potentials. Semi-empirical inelastic cross-sections for heavy- and electron-impact ionization of metals are computed analytically to obtain steric factors. The ionization of sodium is dominant in the production of free electrons, and hyperthermal air–vapour collisions play the most important role in this process. The ionization of air, classically disregarded, contributes to the electron production as significantly as ionization of magnesium and iron. Finally, we propose that DSMC could be employed as a numerical experiment providing ionization coefficients to be used in synthetic models.

Key words: plasmas – methods: numerical – meteorites, meteors, meteoroids.

1 INTRODUCTION

About 100 tonnes of small meteoroids enter the terrestrial atmosphere every day (Love & Brownlee 1993; Vondrak et al. 2008). These bodies, from 1-m diameter to micron-size grains, originate either from sublimating comets or from disintegrated asteroids. In their rush to the ground, they intersect the atmosphere at hypersonic velocities from 11.2 to 72.5 km s^{-1}. As a meteoroid interacts with the atmosphere, its surface temperature can reach several thousands of kelvins, causing its ablation. Bodies up to a few millimetres mainly ablate through melting, i.e. spraying of the molten layer (Girin 2017) and evaporation. The latter is responsible for the metal-rich layers in the mesosphere and lower thermosphere that play an essential role in atmospheric chemical processes (Plane 1991; Plane, Feng & Dawkins 2015).

Due to their small size and tremendous speeds, meteoroids often burn up at high altitudes above 80 km, where the atmosphere is rarefied. Here, the gas cannot be treated under the continuum assumption, and the Navier–Stokes equations usually employed in gas dynamics fail. Moreover, the high energies involved activate coupled physico-chemical phenomena (strong departure from thermo-chemical equilibrium, radiative heating, ionization, and complex gas-surface interactions), which make the prediction of these flows a challenging task (Anderson 2000; Brun 2009).

Ground radar and radio stations are able to detect free electron concentrations in the meteoroid trail (McKinley 1961; Hocking, Thayaparan & Jones 1997; Hocking, Fuller & Vandepeer 2001; Weryk & Brown 2013), which are directly influenced by the ablation mechanism. Ceplecha et al. (1998) estimated that 90 per cent of the meteor light originates from inelastic collisions of vapourized metallic atoms. In fact, the classic formula for the formation of the ionized trail (Jones 1997) reads as

$$q = -\frac{\beta}{\mu V_\infty}\frac{\mathrm{d}m}{\mathrm{d}t}, \tag{1}$$

where μ is the average meteoric atom mass, and quantity q describes the number of electrons produced per meter by an ablating

★ E-mail: federico.bariselli@vki.ac.be

meteoroid of mass m, moving at speed V_∞, only as a function of the ablation rate and the ionization efficiency β. Standard models for these two quantities poorly account for detailed chemistry, diffusion of heavy species in the vapour phase, and rarefied gas effects. Thus, if not accurately determined, they represent major sources of uncertainty.

Classical meteor ablation models were derived under the assumption of free molecular flow and evaporation into the vacuum [see Popova (2004) for a review of the topic]. The simplest among these models assumes that the mass-loss rate is proportional to the kinetic energy imparted to the meteoroid, with the ablation beginning when the surface of the meteoroid reaches its boiling point (Bronshten 1983). Love & Brownlee (1991) proposed an ablation model applying the Knudsen–Langmuir formula

$$\frac{1}{S}\frac{\mathrm{d}m}{\mathrm{d}t} = n_{\mathrm{w}}^{\mathrm{eq}}\sqrt{\frac{\mu k_{\mathrm{B}} T_{\mathrm{w}}}{2\pi}}, \tag{2}$$

in which symbol k_{B} denotes the Boltzmann constant, T_{w} the wall temperature, and S the area of the ablating surface, coupled with the Clausius–Clapeyron relation to compute the equilibrium number density $n_{\mathrm{w}}^{\mathrm{eq}}$ of the melt-vapour phase transition. Campbell-Brown & Koschny (2004) inferred that this model is best suited for meteoroids of lower densities for which the ablation may start before the boiling temperature is reached. This model was adapted by McNeil, Lai & Murad (1998) to treat the differential evaporation of volatile species. Vondrak et al. (2008) adopted a similar approach, with the equilibrium properties of the silicate–vapour system computed by means of mass balance and mass action calculations (Fegley & Cameron 1987).

As reported by Silber et al. (2018a) in their comprehensive review, computational studies in the field of meteor shock waves are relatively sparse with a consequent lack of understanding of the relevant rarefied hypersonic flow. Boyd (1998) was the first to address the problem of the ablation of meteoroids in the rarefied regime by giving a detailed description of the phenomenon from the flowfield perspective using the direct simulation Monte Carlo (DSMC) method (Bird 1994). He treated the meteoroid material as a single species, i.e. magnesium, using a phenomenological ablation model accounting for evaporation of the metal, and assuming a vapourization temperature of 2500 K. No chemical reactions were considered in the gas phase. Preliminary results indicated that a cloud of ablated material surrounds the meteoroid and that an extensive high-temperature region in near-thermal equilibrium is present in the meteor trail. This result is in qualitative agreement with spectral measurements of meteor wakes, but it is not able to predict their composition and ablation rate quantitatively. A DSMC approach was also used by Vinković (2007) to predict the emission of light by very high-altitude meteors detected from the ground, not explainable through classical ablation theory. The study focused on the sputtering of atoms from the meteoroid surface (Rogers, Hill & Hawkes 2005). Strong assumptions were made, such as no distinction between atomic and molecular species in the gas phase. Other physical processes like vapourization, ionization, dissociation, and excitation were not included. A simplified particle-based approach was developed by Stokan & Campbell-Brown (2014) to model the space resolved trail luminosity of faint meteors in direct connection to the local number of collisions.

With application to radar head-echo, Dimant & Oppenheim (2017a, b) developed a simplified kinetic equation to describe the formation of a quasi-neutral plasma around an ablating submilligram meteoroid. They obtained analytical expressions for the spatial and velocity distributions of ions and neutrals, through which they could compute gas and plasma densities as a function of the distance from the meteoroid. Their findings were supported by Particle-in-Cell simulations (Sugar et al. 2018). This type of analysis is valuable to assess the assumptions at the foundations of the classical theory for radio scattering. For example, the degree of attenuation of a radio echo depends on the radial distribution of the electron density within the train. Different authors have argued that the ionization profile is instantaneously formed after the passage of the meteoroid (the so-called *initial meteor radius*, r_0), and it follows a Gaussian distribution around the body (Manning 1958; Greenhow & Hall 1960). Numerical investigation was employed by Jones (1995), who performed some Monte Carlo simulations in the framework of elastic interactions, to show that the ions reach thermal equilibrium in about 10 collisions. Moreover, he found that the initial ionization distribution is far from being Gaussian. According to this author, a more refined description, which takes into account of ionizing collisions, is desirable.

In this work, we aim at providing a detailed description of the ablated vapour dynamics around millimetre-sized meteoroids. Particular attention is given to the modelling of gas-surface interactions and chemical reactions leading to the production of free electrons from heavy-particle and electron-impact ionization of metallic species as well as ionization of air, usually neglected. By doing so, we would like to reduce the initial uncertainties relevant to (i) the input of metals in the chemistry of the upper atmosphere, (ii) the resulting ionization efficiencies which are necessary for the correct interpretation of radar and radio detection measurements. Our analysis is developed in the framework of the DSMC method to account for rarefied gas effects. In particular, an evaporation boundary condition suitable to model multicomponent silicate materials is introduced. The transport properties of the ablated vapour are computed using the Chapman–Enskog theory, and the DSMC phenomenological parameters are retrieved by fitting the collision integrals over a wide range of temperatures. Finally, inelastic cross-sections for heavy- and electron-impact ionization of metals are computed in order to obtain DSMC steric factors.

The paper is structured as follows. In the following section, we give an overview of the meteor phenomenon, focusing on the physical regimes encountered during the hypersonic flight and highlighting the critical limits of currently employed approaches. Physical and numerical models are introduced in Section 3, starting from the boundary condition to end with the computation of elastic and inelastic cross-sections. Finally, in Section 4, the flow around a 1 mm evaporating meteoroid is analysed at different altitudes and velocities so to span different rarefaction regimes.

2 ANALYSIS OF THE FLOW REGIMES

Travelling at geocentric speeds from 11.2 to 72.5 km s^{-1}, meteoroids experience velocities which can be hundreds of times higher than the local speed of sound (Boyd 1998). The bulk of meteoric material vapourizing in the atmosphere is formed by small particles in the range between 5×10^{-5} and 2×10^{-2} m (Ceplecha et al. 1998). Radar and radio waves techniques are able to sample meteoroids smaller than optical systems, but big enough to generate a wake of plasma sufficiently intense to be detected. According to Baggaley (1980, 2002), this corresponds to a rough limit of 10^{-5} m in diameter for meteoroids travelling at a speed of about 30 km s^{-1}. Particles smaller than several hundredths of a millimetre decelerate before reaching the melting temperature. This class of micrometeoroids, for which most of the heat is dissipated by radiation, is not detected neither by radar nor optical techniques

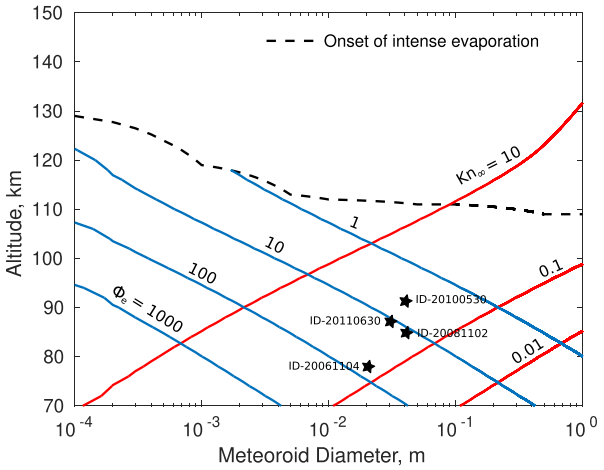

Figure 1. The diagram of the rarefaction regimes encountered by a meteoroid flying at 32 km s^{-1} is shown by plotting the Knudsen number (Kn_∞, red line) and normalized ablation rate ($\hat{\phi}_\mathrm{e}$, blue line) contours in relation to the diameter of the body and the altitude of the detection. The onset of evaporation has been computed through the trajectory analysis performed in Section 4.1. In the plot, four bright meteor events classified between slip and transitional regime are reported (Moreno-Ibáñez et al. 2018).

and disappear into the atmosphere without the possibility of being tracked.

In the picture of a disintegration process mainly driven by evaporation and mechanical removal, ablation only starts after a pre-heating phase in the thermosphere, in which the surface of the body is heated up to the melting condition. In this phase, since the atmospheric density is low, the meteoroid essentially conserves both its mass and flight velocity. The onset of intense evaporation takes place at the altitude at which the surface starts melting. This altitude is a function of the velocity and dimension of the body, with the smallest and fastest meteoroids being vapourized earlier along their trajectory. A quantitative assessment of the onset of the phenomenon will be performed in Section 4.1, in terms of trajectory analysis.

The dynamics of the vapour cloud and its role in the formation of the shock wave is still unclear. Silber et al. (2018a) collected the main analytical, observational, and computational efforts on this topic in their review. Bronshten (1983) extensively analysed the role of the collisions under subsequent levels of approximation to study the effect of screening due to the reflected or evaporated molecules under different conditions. As a result, he obtained values for the drag and heat transfer coefficients (respectively Γ and Λ) to be used under the approximation of free molecular flow. Fig. 1 shows a diagram of the characteristic conditions encountered by a meteoroid in terms of Knudsen number, $\mathrm{Kn}_\infty = \lambda_\infty/D$, where λ_∞ is the mean free path (Bird 1994), and normalized ablation rate, $\hat{\phi}_\mathrm{e}$, as a function of the diameter D and altitude H. From Bronshten (1983), we can write the ablation rate as

$$\frac{\mathrm{d}m}{\mathrm{d}t} = \frac{\Lambda \rho_\infty V_\infty^3}{2L_\mathrm{e}} \pi R^2, \tag{3}$$

where L_e is the latent heat of evaporation and $R = D/2$. Equation (3) is normalized by the initial mass of the object and it tells how much of its initial mass the meteoroid would lose in one second. For example, a 1 mm body falling at 32 km s^{-1}, detected by a radar at an altitude of 90 km experiences free molecular flight, considering that $\mathrm{Kn}_\infty > 10$. However, the collisional regime experienced by the vapour can differ largely from the one suggested by the nominal condition (Silber et al. 2017, 2018b), as evaporation has already been triggered (the point lays below the line of intensive evaporation), and the meteoroid is ablating fast at a normalized rate above 100. In Fig. 1, we also report four bright meteor events among the ones selected by Moreno-Ibáñez et al. (2018). These events are all characterized by an entry velocity around 30 km s^{-1}. Combining infrasound and photometric information with theoretical considerations, three of them were categorized in the slip flow regime and one of them (ID-20100530) at the limit between slip and transitional flow. Here, their position in the diagram places them at a nominal condition of transitional regime ($\mathrm{Kn}_\infty > 0.1$), but in a situation of intense evaporation ($1 < \hat{\phi}_\mathrm{e} < 10$) for ID-20100530, and very intense evaporation ($10 < \hat{\phi}_\mathrm{e} < 100$) for the others.

Due to the large enough number of collisions taking place in the meteor head and vapour cloud, Popova et al. (2000) stressed the importance of taking into account metal–metal interactions in addition to air–metal particle collisions. They stated that, when the vapour pressure is much higher than the atmospheric pressure, the ablated vapour expands similarly to a hydrodynamic flow into a vacuum. In contrast with this suggestion, the methodologies developed by Stokan & Campbell-Brown (2014) and Dimant & Oppenheim (2017a) disregarded the interactions of the evaporated particles with each other. Therefore, we can try to verify this hypothesis by writing the number of collisions per unit time which occur in the vapour cloud as made up by two contributions, air–vapour $\dot{N}_\mathrm{coll}^\mathrm{AV}$ and vapour–vapour $\dot{N}_\mathrm{coll}^\mathrm{VV}$ interactions. It reads

$$\begin{aligned} \dot{N}_\mathrm{coll} &= \dot{N}_\mathrm{coll}^\mathrm{AV} + \dot{N}_\mathrm{coll}^\mathrm{VV} \\ &= 4\pi \int_R^{R^\star} \left(n_\infty n_\mathrm{v} \sigma V_\infty + \frac{n_\mathrm{v}^2}{2} \sigma V_\mathrm{t} \right) r^2 \, \mathrm{d}r \\ &= 4\pi \frac{1-\sqrt{\kappa}}{\sqrt{\kappa}} \left(n_\infty V_\infty + \frac{\sqrt{\kappa}}{2} n_\mathrm{w}^\mathrm{eq} V_\mathrm{t} \right) n_\mathrm{w}^\mathrm{eq} \sigma R^3, \end{aligned} \tag{4}$$

which has been obtained by integrating the collision frequency of the molecules characterized by an average cross-section σ, over a spherical volume around the object of radius R, which spans from its surface to a point in the space where the vapour number density n_v has decayed by a factor κ[1] (at $r = R^\star$). Quantities V_t and n_∞ represent respectively the thermal velocity of the vapour and the freestream number density.

In Fig. 2, quantitative values are given for $\kappa = 10^{-3}$. The contributions of air–vapour and vapour–vapour collisions are studied separately. Above 105 km, vapour–vapour interactions in thermal equilibrium are found to be more important than the interactions with the freestream air molecules. Conversely, hyperthermal air–vapour collisions become dominant at lower altitudes, where the density of the atmosphere is higher.

3 PHYSICAL AND NUMERICAL MODELS

3.1 Statistical description of the gas

As long as the hypothesis of continuum is valid, a hydrodynamic model can be applied (Josyula & Burt 2011). However, under rarefied conditions, the collision rate is too low for the gas to

[1]The underlined hypothesis is that the number density of the vapour decays from its value in equilibrium at the surface temperature, $n_\mathrm{w}^\mathrm{eq}(T_\mathrm{w})$, with the square of the distance r to the wall $n_\mathrm{v} = n_\mathrm{w}^\mathrm{eq} R^2/r^2$, thus $\kappa = (R/R^\star)^2$.

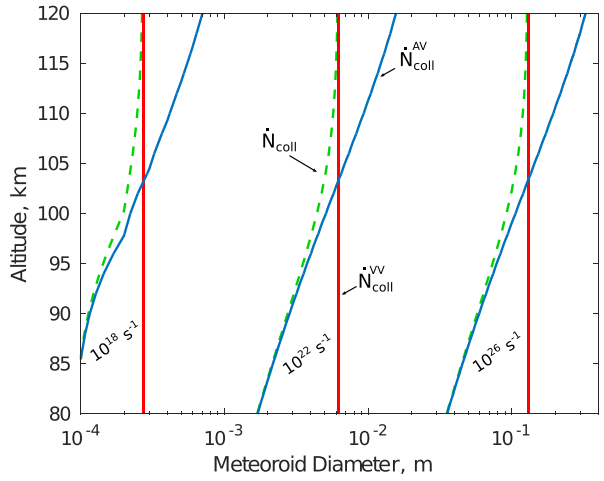

Figure 2. We present the contribution of air–vapour ($\dot{N}_{coll}^{AV}$, blue line) and vapour–vapour ($\dot{N}_{coll}^{VV}$, red line) collisions to the total number of collisions ($\dot{N}_{coll}$, green dotted line) experienced per unit time by the ablated molecules. Contour lines are shown in relation to the diameter of the body and the altitude of detection. Vapour–vapour collisions seem to be very important only above 105 km.

reach local thermodynamic equilibrium. Also, the high energies involved in meteors (above 100 eV) enhance thermo-chemical non-equilibrium effects. Hence, the gas has to be described at the gas kinetic scale, rather than by the Navier–Stokes equations. Such a scale does not allow for a fully deterministic approach, and a statistical description is more suitable. The function $f_i(\boldsymbol{x}, \boldsymbol{\xi}, t)$ is defined as the *one-particle velocity distribution function* for the species i and its evolution over time is described by an integro-differential equation, the Boltzmann equation (Cercignani 1969; Ferziger & Kaper 1972), which for a gas mixture can be written, in the absence of external forces, as

$$\frac{\partial f_i}{\partial t} + \boldsymbol{\xi} \cdot \frac{\partial f_i}{\partial \boldsymbol{x}} = \mathcal{S}_i(f) + \mathcal{C}_i(f) \quad i \in \mathcal{S}, \tag{5}$$

where the left-hand side describes the result of macroscopic gradients on the velocity distribution function in the physical and velocity space $(\boldsymbol{x}, \boldsymbol{\xi})$, whereas $\mathcal{S}_i(f)$ and $\mathcal{C}_i(f)$ are the non-reactive and reactive collisional source terms (Giovangigli 1999).

3.1.1 *Direct simulation Monte Carlo method*

DSMC (Bird 1994) is a particle-based method for the numerical solution of equation (5). This technique has been widely used in the aerospace community over the last 50 yr to simulate hypersonic flows (Ivanov et al. 1998; LeBeau 1999) with a high degree of thermo-chemical non-equilibrium. The trajectories of a representative number of molecules are simulated in the physical space: the particle advection phase is treated deterministically integrating in time the ballistic trajectories, whereas the collisional source terms of equation (5) are solved by means of Monte Carlo stochastic evaluation of the collision pairs. The SPARTA code (Stochastic PArallel Rarefied-gas Time-accurate Analyzer) by Gallis et al. (2014) is used here. Developed at the Sandia Labs, this is an open-source DSMC-Boltzmann solver, and its object-oriented philosophy enables extensions and its usage as an external library.

3.2 Kinetic boundary condition for evaporation

From a microscopic point of view, the vapour–liquid interface is a finite region whose thickness is 10–20 nominal molecular diameters (Frezzotti 2011). At a kinetic scale, its detailed physical structure is neglected and reduced to a surface, Σ, bounding the vapour. The molecular flux of the species i emerging from Σ, which moves at velocity $\boldsymbol{v}_w$ and is characterized by a normal unit vector, $\boldsymbol{n}$, can be modelled by the following inhomogeneous linear boundary condition

$$\begin{aligned} f_i[\boldsymbol{\xi} - \boldsymbol{v}_w] \cdot \boldsymbol{n} \;&=\; g_i[\boldsymbol{\xi} - \boldsymbol{v}_w] \cdot \boldsymbol{n} \\ + \int_{[\boldsymbol{\xi}' - \boldsymbol{v}_w] \cdot \boldsymbol{n} < 0} & \mathcal{K}_{B_i}(\boldsymbol{\xi}' \to \boldsymbol{\xi})\, f_i[\boldsymbol{\xi}' - \boldsymbol{v}_w] \cdot \boldsymbol{n}\, \mathrm{d}\boldsymbol{\xi}', \\ & [\boldsymbol{\xi} - \boldsymbol{v}_w] \cdot \boldsymbol{n} > 0 \quad i \in \mathcal{S}. \end{aligned} \tag{6}$$

This comprises two contributions: (i) the particles coming from the liquid and evaporating into the vapour phase with a half-range Maxwellian. At the equilibrium vapour number density, $n_{w_i}^{eq}$(wall composition, T_w), and temperature, T_w, this distribution can be written as

$$g_i = \frac{\alpha_{e_i}\, n_{w_i}^{eq}}{(2\pi R_i T_w)^{3/2}} \exp\left\{ - \frac{|\boldsymbol{\xi} - \boldsymbol{v}_w|^2}{2 R_i T_w} \right\}, \quad [\boldsymbol{\xi} - \boldsymbol{v}_w] \cdot \boldsymbol{n} > 0, \tag{7}$$

in which R_i is the gas constant defined as k_B/μ_i, k_B being the Boltzmann constant, and μ_i the atomic mass of species i. Departures from equilibrium are taken into account via an evaporation coefficient $0 \le \alpha_{e_i} \le 1$; (ii) the molecules in the gas phase which, interacting with the wall and not condensing, are scattered back and whose velocity is instantaneously changed from $\boldsymbol{\xi}'$ to $\boldsymbol{\xi}$ with probability driven by the *scattering kernel*

$$\mathcal{K}_{B_i}(\boldsymbol{\xi}' \to \boldsymbol{\xi}) = (1 - \alpha_{c_i}) \frac{[\boldsymbol{\xi} - \boldsymbol{v}_w] \cdot \boldsymbol{n}}{2\pi (R_i T_w)^2} \exp\left\{ - \frac{|\boldsymbol{\xi} - \boldsymbol{v}_w|^2}{2 R_i T_w} \right\}. \tag{8}$$

In this case, the kernel is written as if the impinging particles were fully thermalized to the temperature of the liquid. The condensation coefficient $0 \le \alpha_{c_i} \le 1$ represents the probability to condense for a molecule of the species i.

3.2.1 *Melt-vapour system equilibrium properties*

According to equation (7), the distribution functions of evaporating species are determined by the equilibrium vapour partial densities $n_{w_i}^{eq}$. The latter is computed by the multiphase and multicomponent equilibrium solver developed by Fegley & Cameron (1987), MAGMA. Using a mass-action mass-balance algorithm, MAGMA has been widely employed to model silicate lavas and has been extensively validated against experimental data (Schaefer & Fegley 2004).

In the present model formulation, the molten phase is assumed to have constant and uniform temperature T_w as well as constant chemical composition. Therefore, the computed flowfield around the meteoroid is affected by evaporation through the equilibrium vapour densities obtained by MAGMA, but the molten phase composition and temperature are not affected by the computed flowfield.

3.2.2 *Evaporation and condensation coefficients*

Evaporation and condensation coefficients are left as free parameters in the model. For monatomic metal vapours, evaporation coefficients are close to unity (Ogasawara, Tabaian & Maeda 1998).

However, in the case of silicate and oxides, evaporation and condensation involve decomposition and recombination of molecules and atoms. Hence, an activation barrier, associated with the break of bonds in a dissociating and evaporating molecule, may result in rates which are lower than those predicted by the theory. Schaefer & Fegley (2004) reviewed some of the experimental works in which evaporation coefficients for silicate and oxides were computed as the departure of the evaporation rate into vacuum from the equilibrium one. As an example, Hashimoto (1990) reported very low values for the coefficients in forsterite, MgO, and SiO_2. Moreover, numerical efforts by Alexander (2001) and Fedkin, Grossman & Ghiorso (2006) to reproduce experiments by Hashimoto (1983) resulted in species-specific evaporation coefficients far from unity.

In general, little is known about the factors that influence evaporation coefficients and there is no theory for calculating them from first principles. For this reason, we decide to set evaporation and condensation coefficients equal to one for all the metallic species. For nitrogen compounds (e.g. N_2, NO, etc.), the possibility to condense is assumed to be zero. On the other hand, O and O_2, which are both present in the vapour and the freestream, are treated differently: gas-phase oxygen originating from evaporation is assigned a condensation probability equal to one, upon colliding with the meteoroid surface; zero condensation probability is assigned to atmospheric oxygen. In the context of the one-way coupling between molten and vapour phases mentioned above, this rule implements in a very simplified way the assumption that the molten phase is allowed to accommodate by condensation the amount of oxygen lost by evaporation.

3.3 Transport properties of the ablated vapour

Experimental data on transport properties of alkali metal vapours are scarce due to the high temperatures required, low vapour pressures, and corrosive nature (Ghatee & Niroomand-Hosseini 2007).

Kinetic theory provides the mathematical framework which allows linking interatomic forces to transport coefficients. As a result of the Chapman–Enskog perturbative solution method (Bird, Stewart & Lightfoot 1960), the binary viscosity coming from the interaction between species i and j reads as

$$\eta_{ij} = \frac{5}{8}\frac{k_B T}{\Omega_{ij}^{(2,2)}}. \tag{9}$$

Quantity $\Omega_{ij}^{(2,2)}$ is the so-called *collision integral*, defined as

$$\Omega_{ij}^{(2,2)} = \sqrt{\frac{2\pi k_B T}{\mu_{ij}^R}} \int_0^{+\infty}\int_0^{+\infty} e^{-\gamma_{ij}^2}\gamma_{ij}^7(1-\cos^2\chi)b\,db\,d\gamma, \tag{10}$$

in which b is the impact parameter characterizing the binary collision, $\mu_{ij}^R = \frac{\mu_i\mu_j}{\mu_i+\mu_j}$ the reduced mass, and $\gamma_{ij}^2 = \frac{\mu_{ij}^R g_{ij}^2}{2k_B T}$ a reduced variable for the relative velocity g_{ij}. The scattering angle, $\chi = \chi(b, g, \psi)$, resulting from the dynamic of the binary collision, directly depends on the relevant interatomic potential, ψ. Each type of collision (e.g. neutral–neutral, ion–neutral, etc.) would require a different type of potential. However, this procedure quickly becomes cumbersome. In this work, we employ the Lennard–Jones potential

$$\psi(r_{ij}) = 4\epsilon_{ij}\left[\left(\frac{\bar{\sigma}_{ij}}{r_{ij}}\right)^{12} - \left(\frac{\bar{\sigma}_{ij}}{r_{ij}}\right)^{6}\right], \tag{11}$$

which consists of two parts: a steep repulsive term and smoother attractive term. Quantity ϵ_{ij} is the depth of the potential well, $\bar{\sigma}_{ij}$ is the finite distance at which the inter-particle potential is zero, and r_{ij} is the distance between the particles.

Table 1. Lennard–Jones interatomic potential parameters employed to compute collision integrals for neutral–neutral collisions of metallic species.

Interaction	$\bar{\sigma}$ (A)	ϵ/k_B (K)	Reference
Si–Si	2.910	3036.0	Svehla (1962)
Mg–Mg	2.926	1614.0	Svehla (1962)
Al–Al	2.655	2750.0	Svehla (1962)
Fe–Fe	2.468	7556.0	McGee, Hobbs & Baer (1998)
Ca–Ca	4.517	50.000	McGee, Hobbs & Baer (1998)
Na–Na	3.567	1375.0	Svehla (1962)
K–K	4.250	850.00	McGee, Hobbs & Baer (1998)
SiO–SiO	3.516	461.00	Combination rules
SiO_2–SiO_2	3.964	245.94	Combination rules
MgO–MgO	3.527	336.12	Combination rules
Al_2–Al_2	3.345	2750.0	Combination rules
AlO–AlO	3.345	542.00	Combination rules
Al_2O_2–Al_2O_2	4.219	438.75	Combination rules
FeO–FeO	3.235	727.27	Combination rules
CaO–CaO	4.806	59.161	Combination rules
Na_2–Na_2	4.494	1375.0	Combination rules
NaO–NaO	4.004	310.24	Combination rules
Na_2O–Na_2O	4.786	509.61	Combination rules
K_2–K_2	5.354	850.00	Combination rules
KO–KO	4.572	243.93	Combination rules
K_2O–K_2	5.565	369.81	Combination rules

In order to obtain theoretical viscosity curves for single species vapours, we compute $\Omega_{ii}^{(2,2)}$. For this procedure, the Lennard–Jones (6–12) parameters of Table 1 have been employed. Combination rules for polyatomic species, whose potential parameters are not available in the literature, are used as proposed in their work by André et al. (2010)

$$\begin{aligned}\bar{\sigma}_{SiO_2\text{–}SiO_2} &= (\bar{\sigma}_{Si\text{–}Si}^3 + \bar{\sigma}_{O\text{–}O}^3 + \bar{\sigma}_{O\text{–}O}^3)^{1/3},\\ \epsilon_{SiO_2\text{–}SiO_2} &= (\epsilon_{Si\text{–}Si}\,\epsilon_{O\text{–}O}\,\epsilon_{O\text{–}O})^{1/3}.\end{aligned} \tag{12}$$

In Fig. 3, a comparison between our prediction and a few sets of available experimental results (Stefano, Timorot & Totski 1966; Briggs 1968; Lee & Bonilla 1968; Vargaftik et al. 1991) is provided. Differences between theory and experiments may come from the presence of molecules and ions in the vapours or from uncertainties in the potential parameters. One could also argue that the Lennard–Jones potential (6–12) does not apply to alkali metals such as potassium. Ghatee & Niroomand-Hosseini (2007) stated that it fails in the prediction of transport properties of K, Rb, and Cs metals vapour, especially in the low-temperature range. None the less, in our study, the comparison turns out to be fair, with sodium viscosity lying between the two sets of data and the potassium one extremely close. The comparison for atomic potassium thermal conductivity, computed as

$$\lambda_{ii} = \frac{15}{4}\frac{k_B}{\mu_i}\eta_{ii}, \tag{13}$$

is excellent.

3.3.1 *DSMC elastic cross-sections*

In DSMC, the transport properties are the natural result of the simulated binary collisions. DSMC relies on a phenomenological

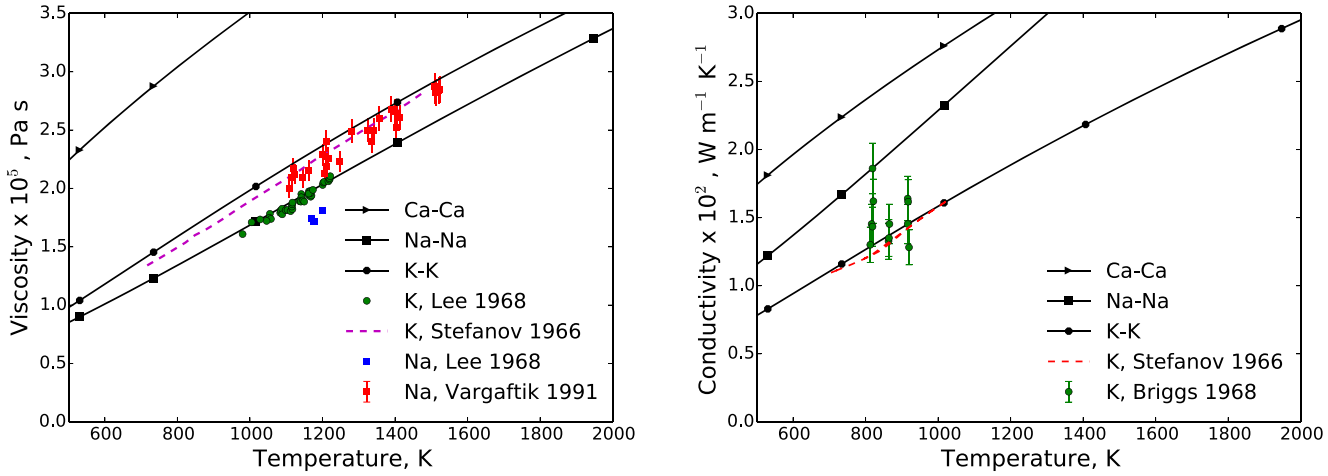

Figure 3. Shear viscosity (a) and thermal conductivity (b) for some alkali atoms and comparison with available experimental data. Ca, which is not an alkali metal, is kept as a reference.

potential to make molecules interact. Although apparently simplistic, these models are able to reproduce to some extent the most salient physics of the collision process, with the advantage of being computationally cheap. In the variable soft sphere (VSS) model, molecules are approximated as rigid spheres of diameter d, which depends on the relative velocity of the impact. The total cross-section is written as

$$\sigma_{\mathrm{T}}\Big|_{\mathrm{VSS}} = \pi d_{\mathrm{ref}}^2 \left(\frac{g_{\mathrm{ref}}}{g}\right)^{2\omega-1}. \tag{14}$$

The quantities d_{ref} and g_{ref} are reference values evaluated at a reference temperature T_{ref}, whereas ω is the temperature exponent which allows the variation of the particle diameter with temperature. In this way, molecules with higher impact energies spend less time interacting on the potential energy surface. In the VSS model, the scattering law reads

$$\chi\Big|_{\mathrm{VSS}} = 2\cos^{-1}\left\{\left(\frac{b}{d}\right)^{1/\alpha}\right\}, \tag{15}$$

which allows to model anisotropic scattering events through the exponent α (where $\alpha = 1$ corresponds to an isotropic scattering law). It is well known that such a model fails in the attempt of capturing diffusion processes in mixtures of gases, and that the anisotropy of neutral-charged collisions in weakly ionized gases is not accurately described (Swaminathan-Gopalan & Stephani 2015). In SPARTA, the collision parameters are obtained by averaging the properties of the collision partners: $d_{\mathrm{ref}_{ij}} = (d_{\mathrm{ref}_i} + d_{\mathrm{ref}_j})/2$, $\omega_{ij} = (\omega_i + \omega_j)/2$, $\alpha_{ij} = (\alpha_i + \alpha_j)/2$. The collision integrals of equation (10), $\Omega_{ii}^{(2,2)}$ can be expressed as function of the VSS model parameters as follows:

$$\Omega_{ii}^{(2,2)}\Big|_{\mathrm{VSS}} = \frac{4\alpha_i}{(\alpha_i+1)(\alpha_i+2)} \frac{\pi d_{\mathrm{ref}_i}^2}{2} \sqrt{\frac{k_{\mathrm{B}}T}{2\pi\mu_{ii}^{\mathrm{R}}}} \left(\frac{T_{\mathrm{ref}_i}}{T}\right)^{\omega_i-1/2} \times \frac{\Gamma(9/2-\omega_i)}{\Gamma(5/2-\omega_i)}, \tag{16}$$

where Γ is the Euler gamma function. Through equation (16), least-squares fitting are performed to obtain the VSS parameters for each collision pair (see Fig. 4). $T_{\mathrm{ref}} = 1000$ K is chosen as reference temperature. The fitting minimizes the error in the range of temperatures between 800 and 4000 K. Table 2 reports the VSS parameters obtained through this procedure.

3.4 Ionization chemistry resulting from hyperthermal collisions

At collision energies above 100 eV, chemical reactions which lead to breaking and formation of new chemical bonds are no longer important processes (Dressler & Murad 2001). Instead, inelastic collisions consisting in transitions to electronically excited atoms are more probable. In particular, in meteors, free electrons are assumed to be mostly produced by collisions of metal atoms with atmospheric molecules through heavy-impact reactions of the following type:

$$\mathrm{M} + \mathrm{N_2} \rightarrow \mathrm{M^+} + \mathrm{N_2} + \mathrm{e^-}, \tag{17}$$

where $\mathrm{N_2}$ can be substituted by $\mathrm{O_2}$. Meteor spectra give an indication in this sense, as they are dominated by atomic lines of meteoric origin, mostly neutral atoms, but also singly ionized ions (Berezhnoy & Borovička 2010). When a sufficient number of electrons has been produced, ionization by electron-impact can take over as the dominant process

$$\mathrm{M} + \mathrm{e^-} \rightarrow \mathrm{M^+} + 2\mathrm{e^-}. \tag{18}$$

Moreover, a substantial contribution to the production of free electrons can be given by photoionization processes of the following type:

$$\mathrm{M} + h\nu \rightarrow \mathrm{M^+} + \mathrm{e^-} \tag{19}$$

and in minor part by secondary impact ionization reactions, involving doubly ionized species. However, only the mechanisms of equations (17) and (18) will be considered in this study.

The most extensive review on the gas-phase chemical dynamics involving metallic species was provided by Dressler & Murad (2001). Although a considerable body of literature exists for thermalized metal chemistry, reliable cross-sections for hyperthermal collisions (1–1000 eV, corresponding to relative velocities of 3–100 km s^{-1}) seem to exist only for Na and K, and a substantial experimental effort would be required (Plane et al. 2015). While ion beam generators are standard technology and the knowledge about

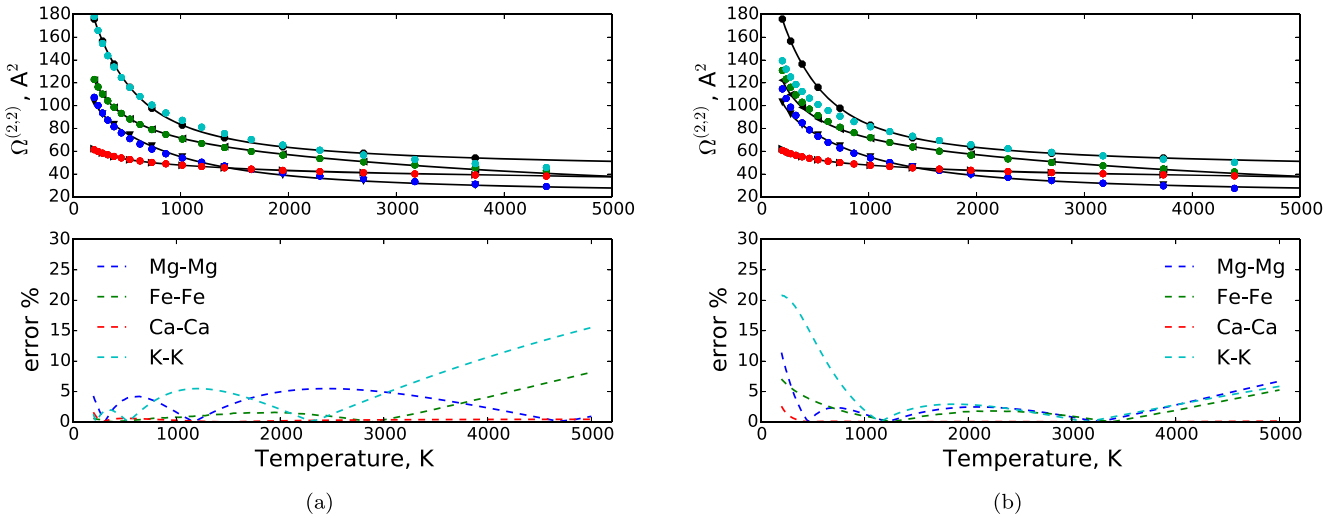

Figure 4. Fitting procedure of the VSS collision integrals with their exact formulation for some metallic atoms. Two possible choices are proposed, (a) to minimize the error between 200 and 5000 K or to (b) minimize the error between 800 and 4000 K.

Table 2. Variable soft sphere parameters obtained by fitting the collision integral $\Omega_{ii}^{(2,2)}$ for $T_{\rm ref} = 1000$ K. This procedure is equivalent to tuning VSS parameters to the viscosity curve. The average fitting error is reported for the range between 800 and 4000 K.

Interaction	$d_{\rm ref}$ (A)	ω (–)	α (–)	Error percent (–)
Si–Si	5.991	0.985	1.293	0.99
Mg–Mg	5.091	0.962	1.370	1.53
Al–Al	5.362	0.991	1.377	0.77
Fe–Fe	5.605	0.869	1.225	1.09
Ca–Ca	4.117	0.648	1.170	0.04
Na–Na	5.865	0.934	1.250	1.86
K–K	5.862	0.830	1.177	2.04
SiO–SiO	4.071	0.721	1.223	1.23
SiO_2–SiO_2	4.140	0.667	1.181	0.48
MgO–MgO	3.847	0.687	1.213	0.80
Al_2–Al_2	6.771	0.991	1.228	0.77
AlO–AlO	4.021	0.744	1.246	1.48
Al_2O_2–Al_2O_2	4.843	0.715	1.168	1.16
FeO–FeO	4.226	0.797	1.276	1.89
CaO–CaO	4.431	0.648	1.183	0.03
Na_2–Na_2	7.377	0.934	1.356	1.86
NaO–NaO	4.318	0.681	1.180	0.71
Na_2O–Na_2O	5.679	0.735	1.176	1.38
K_2–K_2	7.355	0.830	1.450	2.04
KO–KO	4.771	0.667	1.178	0.47
K_2O–K_2	6.180	0.696	1.171	0.92

metal-ion inelastic collisions is relatively established, the same cannot be said of metal–neutral interactions, given the associated experimental difficulties. Friichtenicht, Slattery & Hansen (1967) measured the degree of ionization of fast particles injected into a thick gas target. They found out an approximate $\sim V_\infty^4$ dependence of the ionization cross-sections, higher than the semi-empirical relation $\sim V_\infty^{3.42}$ from Bronshten (1983), but in agreement with the observational investigations by Verniani & Hawkins (1964). The experiments of Bydin & Bukhteev (1960) and Cuderman (1972) provided data on fast alkali neutral metal beams with N_2 and O_2 gases. Although leading to different results, these works showed a similar trend as the O_2 cross-sections resulted in more than an order of magnitude higher than those for N_2. Very few studies (Bukhteev & Bydin 1963; Boitnott & Savage 1971) report measurements of fast Ca, Mg, Si, and Fe collisions in N_2 and O_2 gases, producing cross-sections generally lower than those observed for the alkali metals, whose ionization potentials are inferior. However, the accuracy of these data is questionable.

From the analytical point of view, Kunc & Soon (1991) summarized the available approaches. They show that a reliable theory to predict heavy-impact ionization is not available yet. For this reason, the physico-chemical processes leading to the excitation and ionization of metallic atoms are lumped classically into an ionization efficiency β in function of V_∞, that we have introduced in equation (1) and that is defined as the ratio between the number of electrons produced and the number of vapourized atoms. As shown by Jones (1997), who provides quantitative values, this coefficient can be decomposed into two contributions: the first which represents the proportion of particles β_0 ionizing at the first collision

$$\beta_0 = \frac{c\,(V_\infty - V_0)^2\,V_\infty^{0.8}}{1 + c\,(V_\infty - V_0)^2\,V_\infty^{0.8}}, \tag{20}$$

where the parameter c is a constant calibrated by experimental data and V_0 the ionization threshold velocity; the second that is proportional to $(1-\beta_0)$ and mimics the dynamics of the gas phase, hence the probability with which a collision subsequent to the first one can lead to the formation of an electron.

In this work, we employ Drawin semi-empirical cross-sections (Drawin & Emard 1973) to obtain an estimate of heavy- and electron-impact ionization processes. For the former, the cross-section reads

$$\sigma_{\rm I} = \begin{cases} 0 & \text{if } W_0 < 1 \\ 4\pi a_0^2 \left(\frac{E_{\rm H}}{E_0}\right)^2 \frac{m_{\rm A}}{m_{\rm H}} \xi_0^2 \frac{2m_{\rm e}}{m_{\rm e}+m_{\rm A}} (W_0 - 1) & \\ \quad \times \left(1 + \frac{2m_{\rm e}}{m_{\rm e}+m_{\rm A}}(W_0-1)\right)^{-2} & \text{if } W_0 \geq 1 \end{cases}, \tag{21}$$

where $W_0 = E_{\rm c}/E_0$, $E_{\rm c}$ being the energy of the collision, E_0 the ionization energy, $m_{\rm A}$ and $m_{\rm e}$ the mass of the incident atom and of an electron. $E_{\rm H}$, $m_{\rm H}$, and a_0 are respectively the ionization energy, the mass, and the first Bohr radius of atomic hydrogen. Finally, ξ_0

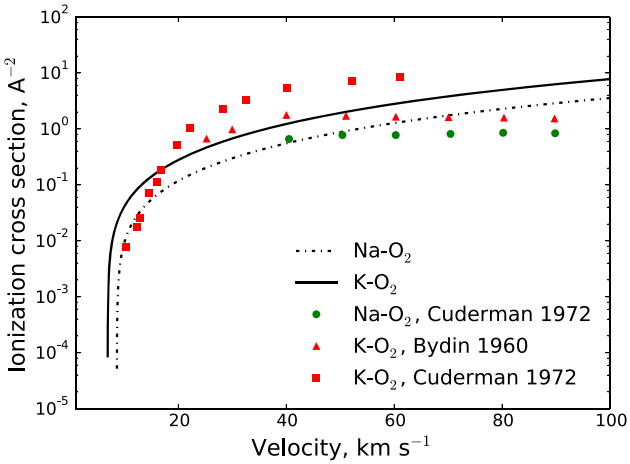

Figure 5. Drawin cross-sections computed for heavy-impact ionization are compared with available experimental data (Bydin & Bukhteev 1960; Cuderman 1972).

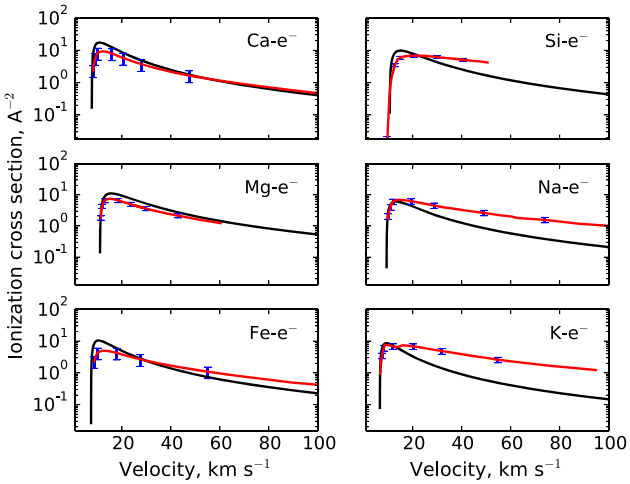

Figure 6. Drawin cross-sections computed for electron-impact ionization (black line) are compared with available recommended data (red line) (Lennon et al. 1988).

represents the number of equivalent electrons in the outer (ground state) shell of the target atom.

In Figs 5 and 6, we provide a comparison of the cross-sections obtained in this work with the experimental results of Bydin & Bukhteev (1960) and Cuderman (1972) for heavy-impact ionization and the data recommended by Lennon et al. (1988) for electron-impact ionization. Results are in reasonable agreement with those reported in the literature. In particular, electron-impact cross-sections by Drawin seem to perform well close to the ionization threshold for all the species. For Si, Na, and K, however, the analytic cross-sections seem to underpredict the recommended values at higher impact energies. Moreover, electron-heavy ionization cross-sections are characterized by a peak not far from the ionization threshold, and after they decrease (Fig. 6). Similarly, this maximum is present in heavy–heavy cross-sections, but it occurs at energy values which are higher than those of interest in this work.

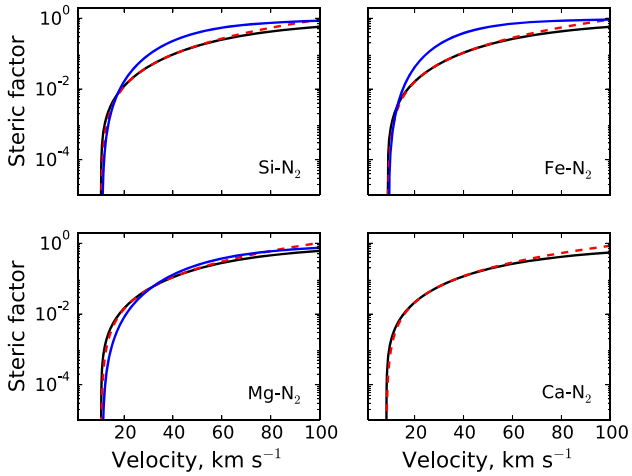

Figure 7. The steric factors computed in this work (black line) and their fitting into a DSMC form (red dotted line) are compared with β_0 coefficients (blue line) (Jones 1997).

3.4.1 DSMC reactive cross-sections

Chemical reactions from the NASA Air-11 mixture, which includes air neutrals and their ions, are accounted for by Park's mechanism (Park 1993; Park, Jaffe & Partridge 2001). This mechanism considers dissociation reactions, in addition to the Zel'dovich process, which can lead to the formation of nitric oxide. The presence of NO in meteor flows has been studied in the past (Menees & Park 1976; Park & Menees 1978; Silber et al. 2018a). Here, it does not represent our focus, as it only marginally influences the electron density. Also, Park's mechanism involves associative and electron-impact ionization of air species and consequent charge exchange reactions.

In SPARTA, chemistry is accounted for through the total collision energy (TCE) method by Bird (1994). This method consists of assuming an analytic form for the collision-dependent reaction cross-section

$$\sigma_{\mathrm{I}}\big|_{\mathrm{TCE}} = \begin{cases} 0 & \text{if } E_{\mathrm{c}} < E_0 \\ \sigma_{\mathrm{T}} C_1 (E_{\mathrm{c}} - E_0)^{C_2} (1 - E_0/E_{\mathrm{c}})^{C_3} & \text{if } E_{\mathrm{c}} \geq E_0 \end{cases}. \quad (22)$$

When averaging this cross-section over a Maxwellian velocity distribution, it is possible to equate it to the known rate coefficient in Arrhenius form. Heavy–heavy and electron–heavy ionization processes of metals have been added to the Park's mechanism. The semi-empirical cross-sections of equation (21) have been fitted into the phenomenological cross-section of equation (22). In SPARTA, the algorithm computes the probability with which a collision can result in a reaction according to a steric factor obtained as the ratio $\sigma_{\mathrm{I}}/\sigma_{\mathrm{T}}$ which, in turn, can be expressed as β_0. A comparison between values of β_0 computed by equation (20) as given by Jones (1997) and the DSMC steric factors obtained in this work is given in Fig. 7, and a fair agreement is found.

TCE coefficients obtained from the fitting procedure for heavy- and electron-impact ionization are presented in Tables 3 and 4.

3.5 Inelastic collisions and plasma effects

The translational-internal energy exchanges for air molecules are modelled according to the classical Larsen–Borgnakke phenomenological model (Borgnakke & Larsen 1975). In this approach, the post-collision properties of the two colliding molecules are sampled

Table 3. TCE coefficients obtained from the fitting procedure of M–N_2 ionization cross-sections. These values can be used for the comparison of the DSMC steric factors with β_0 coefficients, as provided in Fig. 7.

Interaction	C_1 ($1/J^{C_2}$)	C_2 (–)	C_3 (–)	E_0 (eV)
Si–N_2	1.00×10^{-6}	1.23	0.635	8.15
Mg–N_2	7.04×10^{-7}	1.22	0.650	7.65
Fe–N_2	7.49×10^{-8}	1.17	0.695	7.87
Al–N_2	6.01×10^{-7}	1.26	0.635	5.99
Ca–N_2	1.25×10^{-9}	1.09	0.805	6.11
Na–N_2	2.01×10^{-7}	1.24	0.665	5.14
K–N_2	2.75×10^{-8}	1.21	0.715	4.34

Table 4. TCE coefficients obtained from the fitting procedure for electron-impact ionization.

Interaction	C_1 ($1/J^{C_2}$)	C_2 (–)	C_3 (–)	E_0 (eV)
Si–e^-	5.412	−0.51	1.51	8.15
Mg–e^-	2.029	−0.54	1.54	7.65
Fe–e^-	0.027	−0.63	1.63	7.87
Al–e^-	2.299	−0.51	1.51	5.99
Ca–e^-	2.87×10^{-6}	−0.85	1.85	6.11
Na–e^-	0.144	−0.57	1.57	5.14
K–e^-	1.43×10^{-3}	−0.67	1.67	4.34

from a joint equilibrium distribution of translational and internal modes, and the equilibrium relaxation rates are captured tuning rotational or vibrational collision numbers. Also, the excitation of the electronic levels is not taken into account.

Free electrons are treated in SPARTA under the assumption of an ambipolar electric field, which is a standard approximation for low-density plasmas and leads to local charge neutrality (Carlson & Hassan 1992; Boyd 1997). Also, ions are not affected by electric and magnetic fields, and they are characterized by straight ballistic trajectories like neutrals. Similarly, Dimant & Oppenheim (2017a) assumed charge neutrality to develop their kinetic model and neglected the effect of fields on the ions. This assumption was justified by comparing the electrostatic energy with the characteristic ion kinetic energy.

Finally, we do not consider three-body recombination reactions.

4 RESULTS

Ordinary chondrites represent more than 90 per cent of meteorites collected on the ground.[2] Similarly to magmatic rocks such as basalt, these meteorites are composed of a mixture of metal oxides with a composition close to the one reported in Table 5, extracted directly from Vondrak et al. (2008). For our modelling, from here on, this will be considered as the meteoroid prototype.

If the chemical composition of the ordinary chondrites has been widely studied, much less attention has been devoted to characterizing their physical properties, especially at high temperatures (Loehle et al. 2017). The list of the properties employed in this work to model the material is given in Table 6. These properties are assumed in line with those of Vondrak et al. (2008) and Campbell-Brown & Koschny (2004). Finally, thermal conductivity is set according to the work of Yomogida & Matsui (1983), where the authors computed values between 0.415 and 3.85 $W\,m^{-1}\,K^{-1}$.

[2]Metallic meteorites are not found as commonly as chondrites because they oxidize rapidly and are destroyed over time by weathering.

Table 5. Chemical composition chosen as reference for the modelling of an ordinary chondrite (Vondrak et al. 2008).

Oxide	Mass percent	Oxide	Mass percent
SiO_2	34.0	CaO	1.89
MgO	24.2	Na_2O	1.1
FeO	36.3	K_2O	0.1
Al_2O_3	2.5	TiO_2	0.01

Table 6. Physical properties assumed to model an ordinary chondrite.

ρ	($kg\,m^{-3}$)	3500	C_p^L	($J\,kg^{-1}\,K^{-1}$)	1100
k	($W\,m^{-1}\,K^{-1}$)	3.5	T_m	(K)	2000
ϵ	(–)	1.0	L_m	($J\,kg^{-1}$)	4×10^5
C_p^S	($J\,kg^{-1}\,K^{-1}$)	1050	L_e	($J\,kg^{-1}$)	4×10^6

4.1 Trajectory analysis

First, we consider the thermal response of the meteoroid along its entry trajectory by solving the equations reported in Appendix A, obtained by compiling the works by Ceplecha et al. (1998) and Bonacina et al. (1973). This synthetic analysis has the aim of providing relevant boundary conditions for the gas phase simulations, for both the freestream and the surface. This is important for two reasons. First, the rate of evaporation of metallic species, which is the primary source of free electrons, is a strong function of the temperature of the body. Secondly, we are interested in estimating the altitudes at which the evaporation is onset and for which the dynamics of the vapour could play a significant role.

Trajectory simulations are run for different diameters (1, 2, 5×10^{-3} m) and velocities spanning from 12 to 72 $km\,s^{-1}$. The simulations are compared with data stored in the Japanese Meteor Science Seminar Working Group (MSSWG) Orbit Database, where multistation video meteor data have been collected over 26 yr. These data are freely available for download on the International Meteor Organisation website (IMO). Some data are reported in Fig. 8, showing the onset of the meteor phenomenon and its extinction. As a modelling assumption, we assumed that these two points correspond respectively to the beginning and the end of the ablation process. Average values and standard deviations are also reported. A radiant angle $z_R = 40$ deg, which turns out to be the most probable from the data base, has been chosen along with drag coefficient, $\Gamma = 1$, and heat transfer coefficient, $\Lambda = 0.5$ (Campbell-Brown & Koschny 2004).

In Fig. 8, results from the synthetic model appear in the range of two standard deviations of the MSSWG observation. Slower simulated meteoroids seem to present longer trajectories than the observed ones. A possible explanation could reside in the fact that, for slower bodies, characterized by lower rates of evaporation, the entrainment of the molten layer by the surrounding gas may represent a significant mechanism of mass-loss, which is not modelled here.

When a meteoroid enters the atmosphere, it starts heating up very quickly. However, down to 200 km, the rise in temperature of the body is generally small. Particles of size 10^{-4} m are characterized by fast and uniform heating with negligible temperature gradients

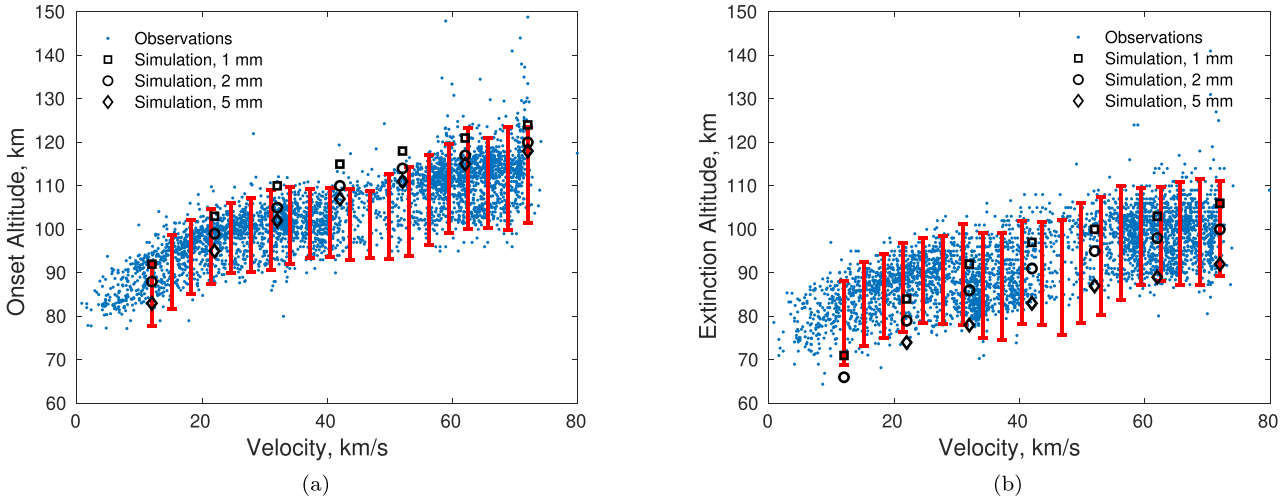

Figure 8. Altitude of onset (a) and extinction (b) of the meteor from the visual detections stored in the MSSWG Orbit Database (IMO). The comparison with the simulated trajectories shows a good agreement with the observational data.

between the surface and the core of the body. The cooling effect due to the re-radiation of the surface is evident for the smaller and slower particles. For this condition, the melting temperature is not reached, and the body cools down as soon as the meteoroid starts decelerating. As shown in Figs 9(b) and (c), the thermal non-equilibrium inside the material is enhanced by increasing the velocity and the diameter. For bigger bodies (Fig. 9c), the thermal response is delayed, and the rise in temperature occurs abruptly.

When the surface starts melting, evaporation can commence. From this point of the trajectory on, the energy is dissipated mostly by evaporation, and the material does not heat up any more. Only higher heat fluxes (Fig. 9d), encountered at greater velocities, lead the surface temperature to overcome the melting condition. This plateau could also be due to the chemical composition of the meteorite, kept constant along the trajectory. A depletion in volatile elements in the first part of the simulation would probably result in a drop of the vapour pressure (because dominated by the refractory elements) with a consequent increase of the surface temperature (McNeil et al. 1998; Janches et al. 2009). On the other hand, Fig. 9(a) reveals a condition for which the object stops ablating before being completely disintegrated and glides down to the lower atmosphere layer as it loses momentum.

When small particles start melting, they immediately become molten droplets (see Fig. 9a). In this condition, the effect of the flow shear may play an important role, with the mass being lost mainly through mechanical removal (Girin 2017). In particles of intermediate size (see Figs 9a and b), a layer of liquid develops over the solid particle. This layer seems not to be present in the largest and fastest class of bodies under study (see Fig. 9d), where the evaporation front consumes the molten film, and the two fronts turn out to coincide. Moreover, in this class of meteoroids, heat conduction does not have time to level out the temperature inside the body, and the core remains unaffected. It is reasonable to think that this class of meteoroids fragments due to the large thermal stresses at the surface.

4.2 Flowfield analysis

We are interested at providing a picture of the steady flowfield at a certain instant along the trajectory, at a given chemical composition and temperature of the condensed phase. We start with a numerical test conceived to assess the degree of thermal non-equilibrium in a rarefied hypersonic flow at velocities and sizes relevant for the meteor phenomenon.

Then, as main study case, we investigate the flow around a 1 mm meteoroid, flying at 32 km s^{-1}, at three different altitudes: 80, 100, and 120 km. We base on the fact that, in Fig. 8, the altitude of detection roughly spans from 80 to 120 km. The surface temperature is set to 2000 K. This value is chosen in agreement with the results of previous Section 4.1, in which, after the onset of the evaporation, the wall temperature reveals a plateau not far from the melting condition independently from the initial size and velocity. However, in Section 4.2.5, we examine the effect of the wall temperature on the flowfield at 80 km altitude, for the case in which $T_w = 3000$ K.

Lastly, in Section 4.2.4, we study the details of the ionization process and extract global ionization efficiencies from the simulations at different altitudes (80, 100, and 120 km) and flight velocities (12, 32, and 72 km s^{-1}), which could be used as input in classic synthetic models.

4.2.1 Details of the simulations

The simulations are performed in a 2D axisymmetric configuration around a spherical body. The wall is assumed fully catalytic for ion–electron recombination. Freestream densities, compositions, and temperatures are computed according to the Naval Research Laboratory Mass Spectrometer Incoherent Scatter Radar (NRLMSISE-00) empirical atmospheric model developed by Picone et al. (2002).

In Fig. 10, we show the equilibrium composition of the vapour in a relevant range of temperatures. At 2000 K, the ablated vapour is mainly composed of O, O_2, Fe, FeO, Na, and NaO, while SiO, SiO_2, Mg, and MgO appear only at higher temperatures. K, which is only present as a trace element in the liquid phase, is not considered in the simulations, given the difficulties to accurately track minor

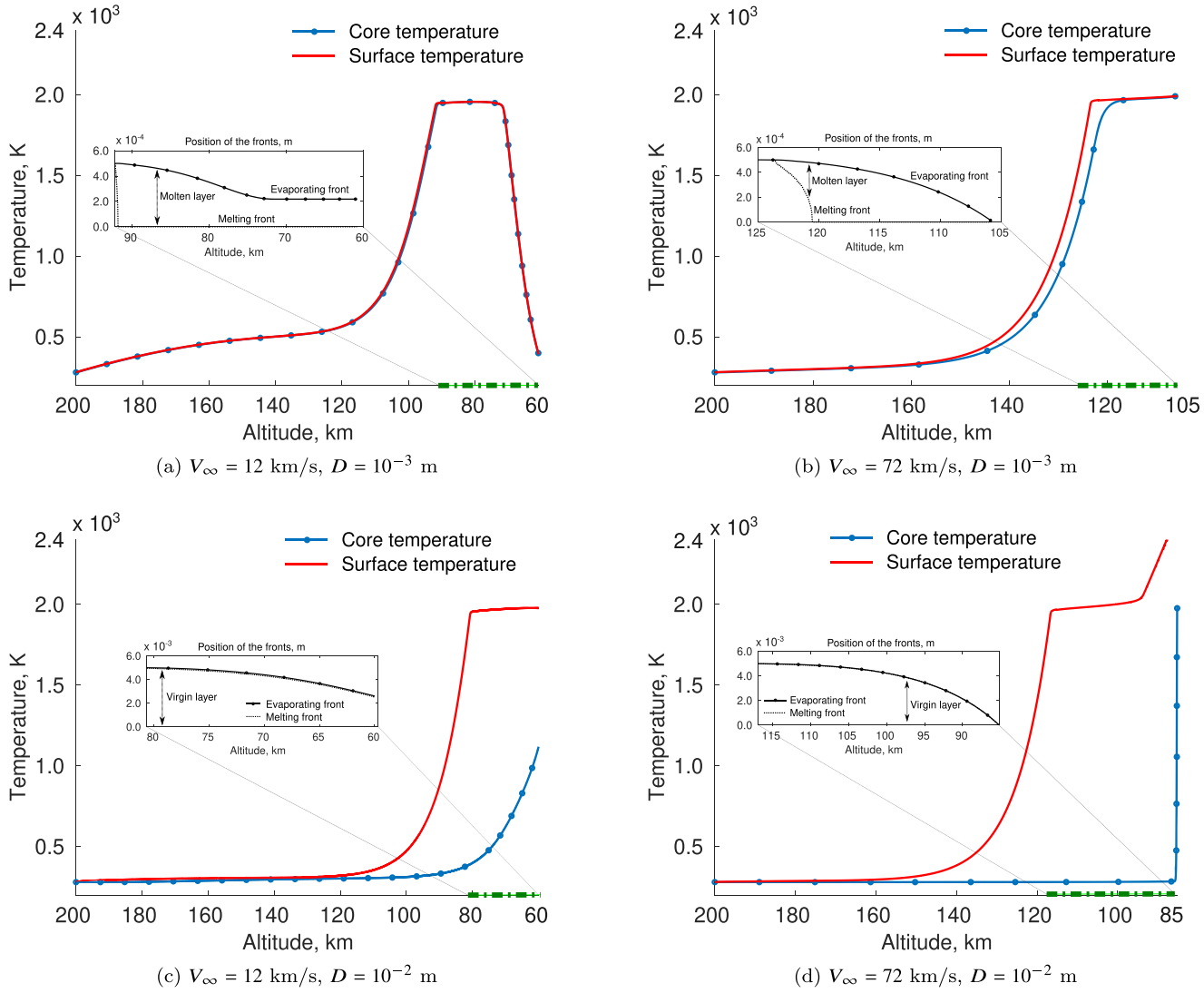

(a) $V_\infty = 12$ km/s, $D = 10^{-3}$ m

(b) $V_\infty = 72$ km/s, $D = 10^{-3}$ m

(c) $V_\infty = 12$ km/s, $D = 10^{-2}$ m

(d) $V_\infty = 72$ km/s, $D = 10^{-2}$ m

Figure 9. Temperature and fronts evolution along the simulated trajectories, for a range of diameters D and velocities V_∞, typical of meteoroid entry. The positions of the melting and evaporation fronts are computed from the core of the body.

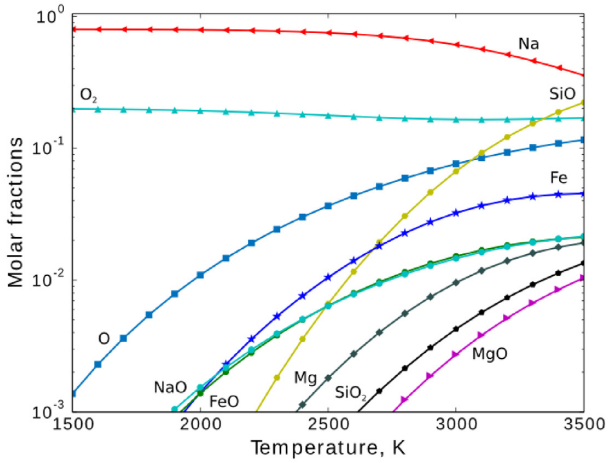

Figure 10. The composition of the ablated vapour in equilibrium with its condensed phase is shown for a range of temperatures characteristic of meteoroid melting. The results are obtained with the software MAGMA (Fegley & Cameron 1987).

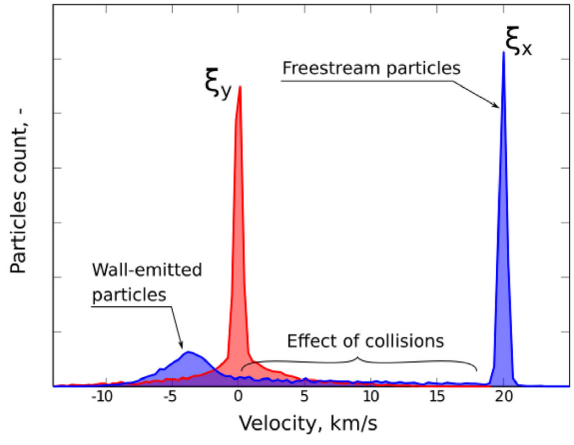

Figure 11. VDF for the axial (ξ_x) and radial (ξ_y) velocities in front of a 1 cm body flying at 20 km s^{-1}. Two populations are visible in the axial VDF, shifted with respect to each other by a hypersonic velocity: the freestream and the wall scattered molecules. The same populations, with zero average velocity but the same temperature, can be distinguished from the radial VDF.

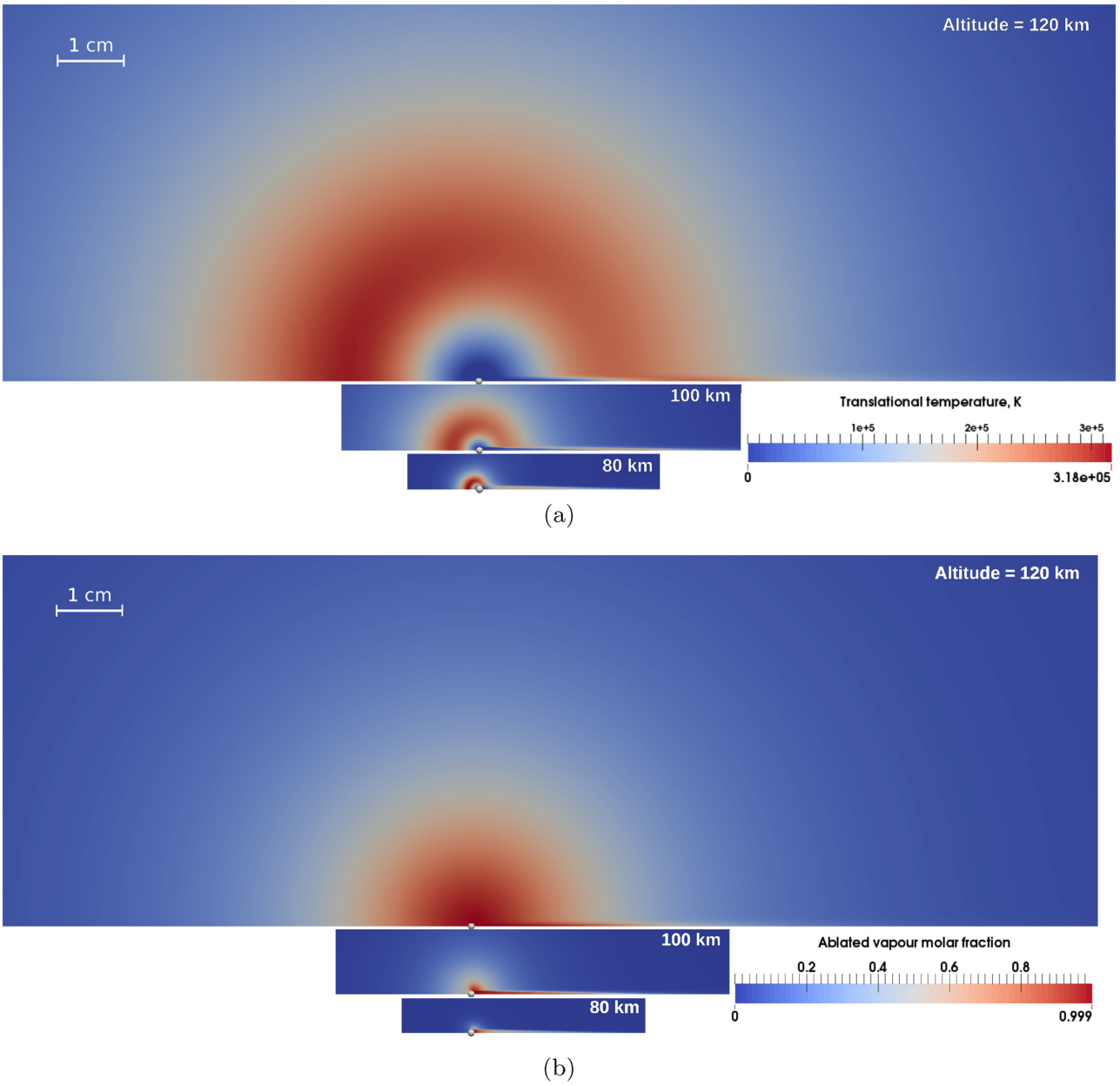

Figure 12. Fields for the translational temperature (a) and the ablated vapour molar fraction (b) for three different altitudes of detection: 80, 100, and 120 km. The wall temperature is 2000 K, the diameter of the body 1 mm, and its velocity 32 km s^{-1}. The freestream flows from left to right.

species in DSMC. Moreover, refractory elements such as Ca, Al, and Ti are excluded from the simulations as they do not significantly contribute to the evaporation process at these temperatures.

4.2.2 Investigation of thermal non-equilibrium in the gas phase

We consider a 1 cm body, flying at 20 km s^{-1}. We extract the velocity distribution function (VDF) from DSMC simulations. The front region (Fig. 11) shows a very high degree of non-equilibrium: the freestream particles (seen as a sharp peak at 20 km s^{-1}) are easily distinguished from the scattered molecules (with a Maxwellian distribution characterized by negative velocities). The effect of collisions is slightly visible, populating a region that connects the two families of particles. The resulting axial VDF has a bimodal shape, and the temperature anisotropy between the axial and radial translational modes can be appreciated.

4.2.3 Influence of the altitude on the dynamics of the gas phase

Now, we consider a 1 mm meteoroid at three different conditions: 80, 100, and 120 km. The comparison of translational temperatures and concentrations of the ablated vapour are shown in Fig. 12. First of all, in Fig. 12(a), we see a rise in the temperature in front of the body. This growth becomes more and more diffuse as the freestream density decreases, and the bow shape, well visible at 80 km, gradually disappears. As a result of the thermal non-equilibrium, very high temperatures are computed. In DSMC, these temperatures are related to the width of the overall VDF which comes from the blending of the distributions of the two different

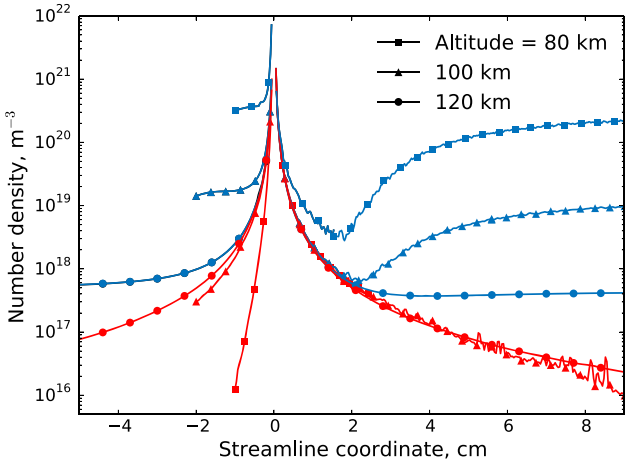

Figure 13. Density profiles along the axis of symmetry for three different altitude conditions. The reference system is centred at the stagnation point: air–vapour mixture (blue line), ablated vapour (red line).

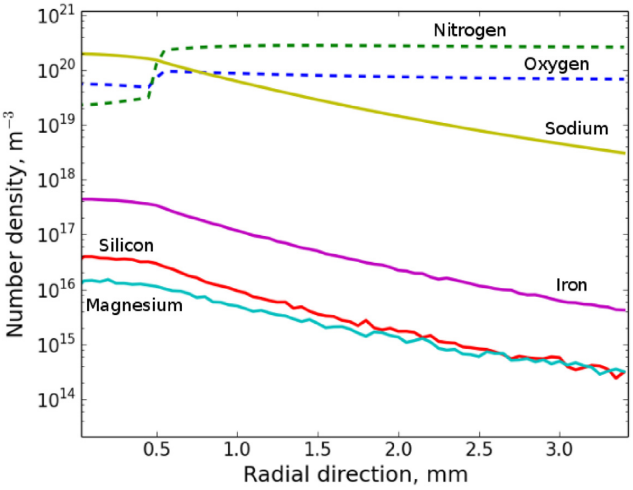

Figure 14. Density profiles in the radial direction in the rear of a 1 mm body flying at a speed of 32 km s^{-1} at 80 km altitude. Labels in the plot refer to the species associated with a single element, e.g. sodium (Na, Na$^+$, NaO), silicon (Si, Si$^+$, SiO, SiO$_2$), nitrogen (N, N$^+$, N$_2$, N$_2^+$), etc.

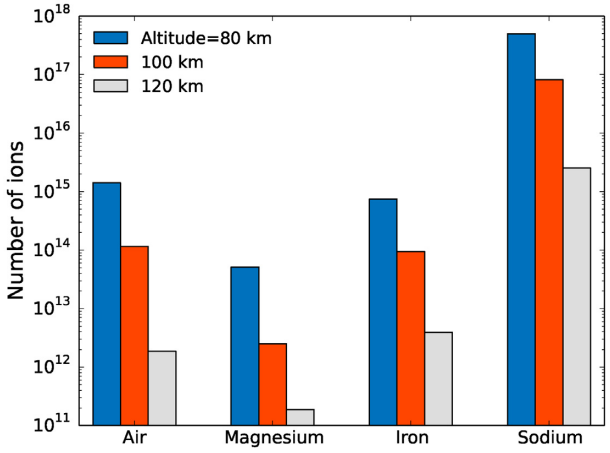

Figure 15. Number of ions generated by gas-phase collisions at different altitudes. The process is dominated by sodium. Air ions are always comparable with Mg$^+$ and Fe$^+$.

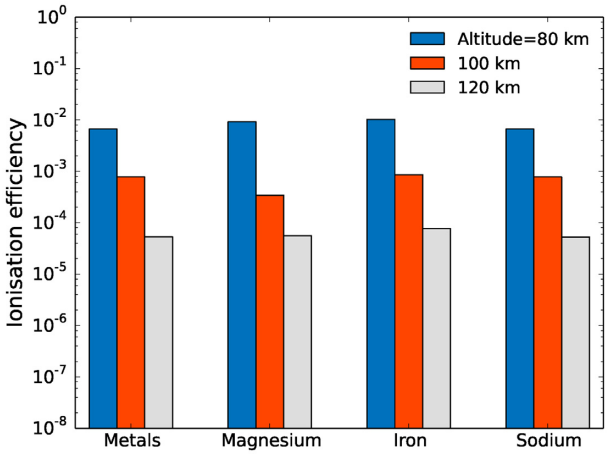

Figure 16. Global and species-specific ionization efficiencies computed according to equation (24) at different altitudes. The wall temperature is 2000 K. The resulting ionization efficiency inside the computational domain is a strong function of the altitude.

classes of molecules. This effect has been described in Section 4.2.2 in terms of microscopic quantities for a non-ablating body, and it was already observed by Boyd (1998). As a result, no particles are really characterized by such a temperature in the thermal sense. The scarce effect of collisions is also confirmed by the fact that the maximum value of the temperature seems insensitive to changes in the altitude: in fact, as the amount of collisions decreases, internal molecular modes become less excited, and the gas starts behaving like a monatomic gas, characterized only by translational degrees of freedom.

At 120 km, the ablation phenomenon resembles a spherical expansion into the vacuum, with the ablated vapour able to travel upstream, only marginally interacting with the incoming jet. In this condition, a metal cloud forms all around the body, in almost spherical symmetry (see also Fig. 13). The pressure of this vapour is higher than the stagnation pressure generated by the air molecules. At 100 km, the density profile of the ablated vapour along the stagnation line is very similar to the one at 120 km, but still different in terms of molar fraction (compare Figs 12b and 13). On the other hand, at 80 km, the concentration of metals ahead of the body is less important and leads to two possible considerations. First, the vapour is taken away by the incoming jet. Secondly, the ablated atoms are immediately scattered back towards the wall where they can condense. In Fig. 13, the metal vapour profiles are the same in the trail for all the tested conditions. This is because the close trail would be nearly in vacuum if it were not for the ablated vapour.

Finally, number density profiles along the radial direction in the rear of the body are plotted in Fig. 14 at an altitude of 80 km. In this picture, we have lumped the species into groups associated with the related chemical element. The mixing layer at the edge of the trail is evident if we look at the air species profiles. Concentrations reflect the vapour pressures computed by MAGMA. The ablated vapour fills the trail and diffuses in the background gas. Silicon and magnesium profiles are in close concentrations.

Heat transfer coefficients: In order to assess the shielding effects by the ablated vapour, the heat transfer coefficient is computed as follows:

$$\Lambda = \frac{\dot{q}_s^{\mathrm{DSMC}}}{1/2\ \rho_\infty\ V_\infty^3}, \tag{23}$$

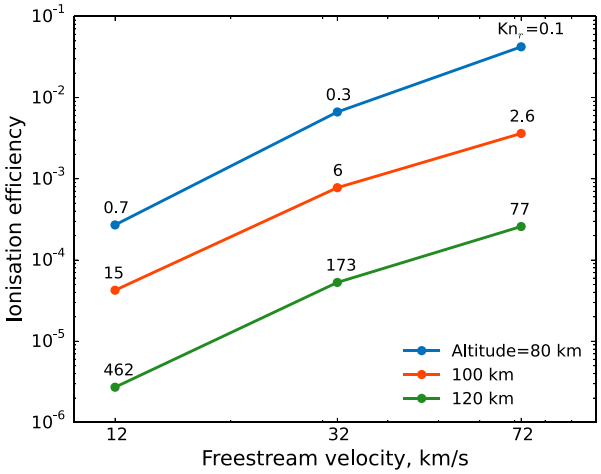

Figure 17. Global ionization efficiencies computed inside the computational domain according to equation (24), at different altitudes and freestream velocities. The wall temperature is 2000 K.

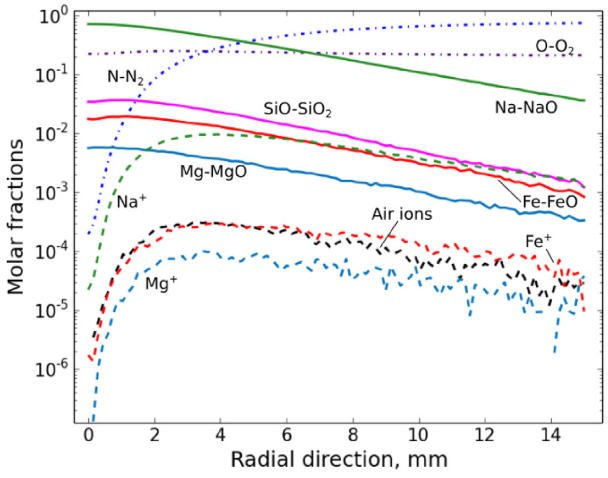

Figure 18. Concentration profiles in the radial direction in the rear of a 1 mm body flying at a speed of 32 km s^{-1} at 80 km altitude, and ablating at a surface temperature of 3000 K.

where $\dot{q}_s^{\mathrm{DSMC}}$ is the numerical heat flux measured at the stagnation point. For all the conditions, we find that $\Lambda \approx 1$, meaning that the evaporation flux at 2000 K is not intense enough to partially screen the meteoroid from the energy of the incoming flow. The scenario will change radically in a condition of stronger evaporation, like the one we will analyse in Section 4.2.5.

4.2.4 *Production of free electrons*

A cylindrical volume of ionized plasma quasi-instantaneously forms upon the passage of the meteoroid. Literature refers to the radius of this cylinder as the *initial meteor radius*, which is usually defined as the half-width of the initial Gaussian distribution of electrons (Manning 1958). In the determination of r_0, Jones (1995) assumed that the vast majority of the metal atoms ionize after the first collision. However in DSMC, if the first collision is elastic, the ablated particle may experience a fully elastic thermalization during subsequent interactions with the surrounding atmosphere, as the atom loses about one-third of its speed after each collision. Although we cannot say much about the length of this radius (our computational domain is only few meteoroid diameters wide), the conducted analysis provides an insight on the formation of the plasma and on its radial distribution.

Electrons are mainly produced ahead of the body and are advected around the meteoroid to the rear, where they start to dissipate by diffusing in the low-density surrounding (see Fig. 21). We are assuming that recombination plays a significant role only in the long trail, which is not part of the simulated domain.

Up to 40 km s^{-1}, heavy-impact ionization cross-sections are smaller than those for electron-impact ionization (the reader can compare Figs 5 with 6). However, the former process is necessary to trigger the electron avalanche. In Fig. 15, we see that the contribution of Na to electron production is prevailing.

Between 80 and 120 km, a difference between 2 and 3 orders of magnitude exists in the number of free electrons (Fig. 15). If we now look at a single element, we can appreciate the influence of the Knudsen number on the ionization process. The number of generated ions is a strong function of the altitude of detection, although the number of their parent neutrals is the same for all the conditions, as it only depends on the wall temperature and meteorite composition. However, equation (1) cannot capture this behaviour as the electron density only depends on the energy of the collisions, through V_∞, and the ablation rate. In fact, in classical models, the effect of the density of the incoming jet enters the physical description only in the material energy balance. We will come back to this point later in the discussion about the ionization coefficients.

In the same plot, we can compare the ionization degree between metals and air species. The number of ions coming from the air (N^+, O^+, N_2^+, O_2^+, and NO^+) is always comparable with those of Mg and Fe. This aspect is disregarded by standard models which assume metals as the only responsible for the plasma formation.

Ionization efficiency in the simulated domain: For each metal, we can now use the following definition:

$$\beta_i = \frac{N_i^{\mathrm{ions}}}{N_i^{\mathrm{ions}} + N_i^{\mathrm{neutrals}}}, \tag{24}$$

in order to extract the resulting equivalent efficiency of the ionization process in the simulated domains.

Fig. 16 shows that metals present similar ionization coefficients at a given condition. On the other hand, efficiency is strongly dependent on the altitude. We have previously mentioned this effect in the count of the generated ions (Fig. 15). To further investigate this, we perform nine simulations at different altitudes (80, 100, and 120 km) and flight velocities (12, 32, and 72 km s^{-1}).

Ionization efficiencies for all the conditions are reported in Fig. 17, along with the Knudsen number experienced by the evaporating molecules relative to the impinging jet

$$\mathrm{Kn_r} = \sqrt{2}\frac{V_t}{V_\infty}\mathrm{Kn}_\infty, \tag{25}$$

as proposed by Bronshten (1983), where V_t represents the thermal velocity of the ablated atoms leaving in equilibrium with the wall. The dependence of the ionization efficiency from $\mathrm{Kn_r}$ is apparent. Flows with higher V_∞ experience greater collisional frequencies for the same Kn_∞. In general, coefficients in Fig. 17 appear to be much lower than those proposed by Jones (1997)

$$\beta \approx 9.4 \times 10^{-6}(V_\infty - 10)^2 V_\infty^{0.8}, \tag{26}$$

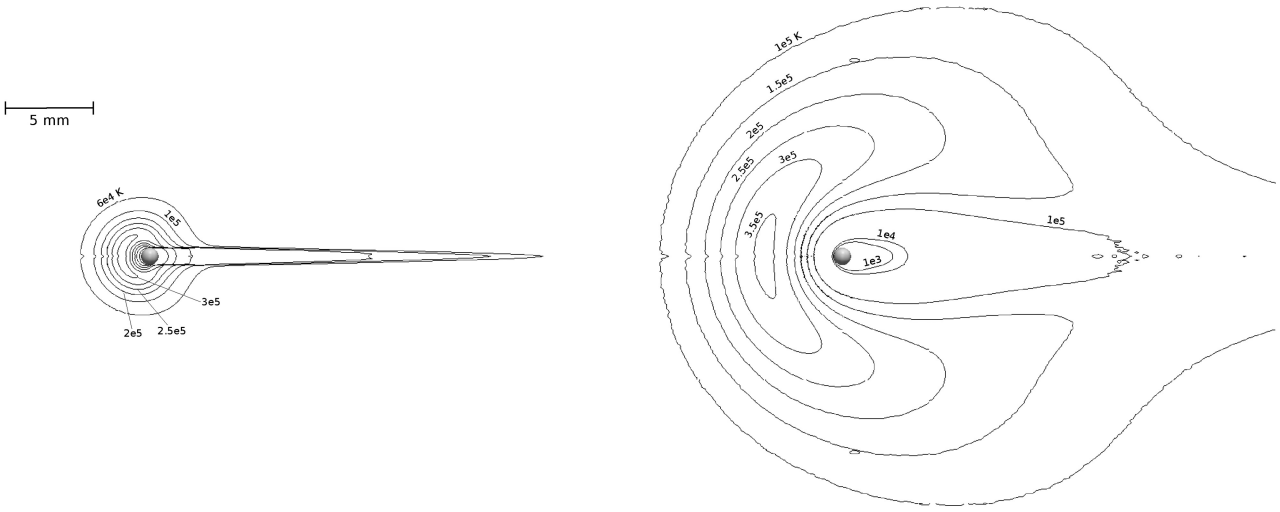

Figure 19. Translational temperature at 80 km altitude for 1 mm body flying at 32 km s^{-1}. Comparison between two different evaporation regimes, T_w = 2000 K (left) and 3000 K (right). The freestream flows from left to right.

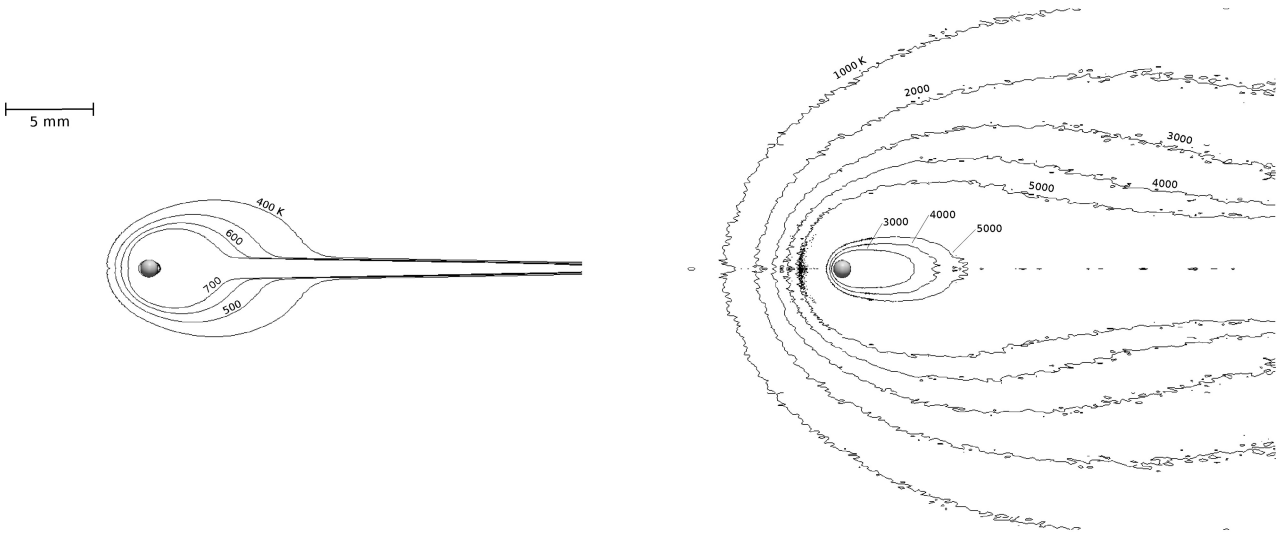

Figure 20. Vibrational temperature at 80 km altitude for 1 mm body flying at 32 km s^{-1}. Comparison between two different evaporation regimes, T_w = 2000 K (left) and 3000 K (right). The freestream flows from left to right.

where the freestream velocity is expressed in km s^{-1}. However, a direct comparison between equation (26) and Fig. 17 is not appropriate as it would require to simulate much wider domains. Independently from the degree of rarefaction, the metallic atoms may take a few mean free paths to ionize. Therefore, to obtain values that could be directly used for radio and radar observations, the collection of the electrons should be done from a domain of the order of the electromagnetic wavelength employed in the detection which, in turn, could be used to define a relevant macroscopic length for the Knudsen number.

None the less, a severe discrepancy between his theoretical work and observational fits was found by Jones (1997), according to whom equation (26) may be useful to interpret laboratory results in ionization chambers at air densities higher than those of the upper atmosphere, but its use to investigate meteor observations could be improper.

4.2.5 *Influence of the wall temperature on the flowfield*

In order to analyse the influence of the evaporation regime on the overall flowfield, we now perform a simulation for a 1 mm meteoroid flying at 32 km s^{-1}, at an altitude of 80 km, and ablating at a surface temperature of 3000 K.

Atomic sodium and its ion still dominate the ablated vapour, but all the other metal species are present in relevant concentrations (see Fig. 18), except for Si which is not visible in our simulations as its saturated pressure is too low. In reality, however, the latter would be probably generated by the break of the bonds of SiO and SiO_2 molecules, whose dissociation reactions are not included in this work. Ions profiles plotted in Fig. 18 present a similar behaviour in that they reach a maximum value just outside of the trail (now several diameters wide). This reinforces the idea for which the ionization process is mainly driven by the energetic collisions between the incoming air jet and the vapour.

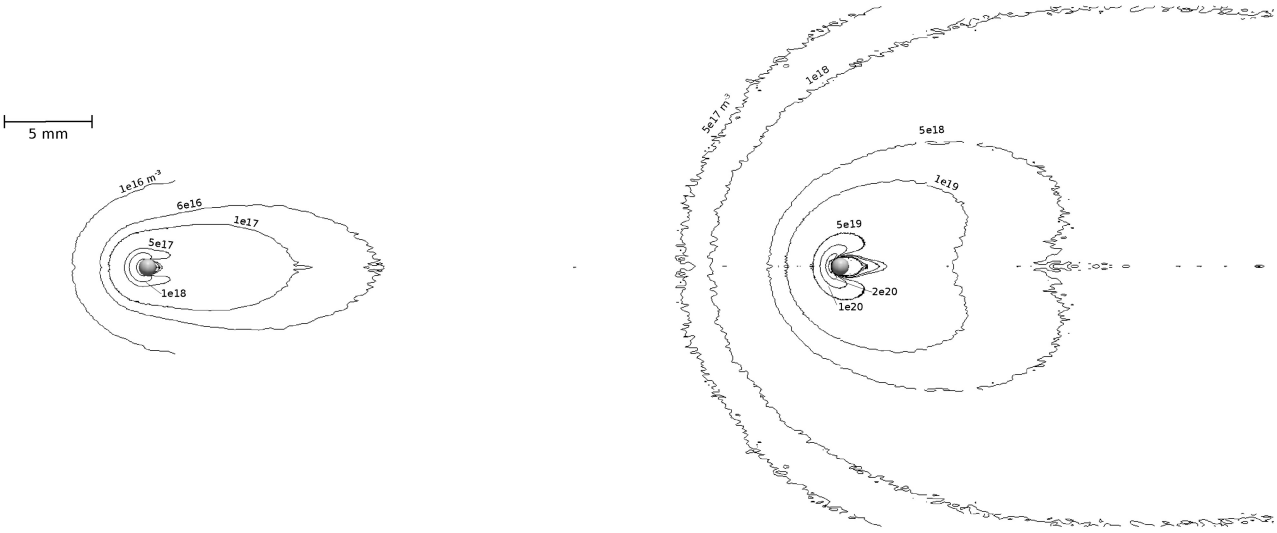

Figure 21. Electron number density at 80 km altitude for 1 mm body flying at 32 km s^{-1}. Comparison between two different evaporation regimes, T_w = 2000 K (left) and 3000 K (right). The freestream flows from left to right.

Fig. 19 shows that the ablation rate is preeminent in the outcome of the simulation. As the saturated vapour pressure varies exponentially with the wall temperature (Clausius–Clapeyron law), evaporation is much stronger at this condition and results in a region of perturbed atmosphere which is considerably wider than in the case previously studied.

In Fig. 20, the excitation of the vibrational degrees of freedom is important (up to 6000 K) for both the situations, although for the case of intense evaporation, the region of excitation left behind by the meteoroid is much more extensive, and the vapour ablating from the sides of the body significantly contributes to the excitation process.

Similar conclusions can be drawn by analysing Fig. 21, reporting contours for free electrons number densities. Here, electron densities reach peak values above 3×10^{20} m^{-3} at the stagnation point for $T_w = 3000$ K (compared to 1×10^{19} m^{-3} for the case of moderate evaporation), but high degrees of ionization occur in the whole surrounding of the body, and they become remarkably significant at the sides of the meteoroid.

Finally, at this condition, the vapour relevantly screens the meteoroid from the incoming air, and this translates in low values of the heat transfer coefficient, $\Lambda \approx 0.25$.

5 CONCLUSIONS

DSMC is an established method for the study of transitional flows, where the hydrodynamic regime does not hold, and analytical solutions cannot be found. Hence, it represents an excellent technique for the study of meteor flows, not least for the simplicity with which it is possible to include physico-chemical models in the algorithm. None the less, DSMC developers should look at meteors in the attempt to extend, train, and ultimately validate their models in the presence of a high degree of thermo-chemical non-equilibrium.

We have used DSMC to analyse the detailed flowfield structure in the surroundings of a meteoroid at different conditions, spanning a broad spectrum of Knudsen and Mach numbers. For this purpose, an evaporation boundary condition has been employed relying on a multicomponent multiphase equilibrium solver. With respect to the usual approach, this boundary condition can take into account condensation fluxes and the backscattering of molecules at the wall.

Secondly, we have computed the transport properties of the metals in the gas phase starting from Lennard–Jones potentials. These new data have enabled comparison with experimental values for viscosities and thermal conductivities available in the literature for some neutral alkali species. Moreover, DSMC inelastic cross-sections have been derived based on Drawin's methodology, and the link with the classical theory on ionization efficiencies has been provided. This set of data, comprising of elastic and inelastic cross-sections, may result to be useful to scientists as a reference data base for future theoretical and numerical studies and can be used independently from the DSMC method.

According to the preliminary trajectory analysis, we have decided to model the flow around a 1 mm meteoroid evaporating, not far from its melting condition. A high level of thermal non-equilibrium has been measured in the head of the meteor. At higher altitudes, the vapour can travel upstream without interacting much with the incoming jet. On the other hand, the interaction between the vapour and the incoming jet is significant at 80 km, especially in the condition of intense evaporation.

The ionization of sodium turned out to be the dominant process in the production of free electrons, and hyperthermal air–vapour collisions play the most important role in this process. The ionization of air species, which is not considered by the classical theory of meteors, is always comparable, if not higher, to the one of Mg and Fe. We have also proposed a methodology through which DSMC can be employed as a numerical experiment to provide ionization coefficients to be used as input in synthetic models.

Future work will focus on the modelling of chemical and diffusion processes of the meteor trail, which offers a set of additional challenges. The most important one concerns its vast extent, which can reach several hundreds of metres. Numerical simulations of such a thin and elongated geometry would not be feasible using standard DSMC tools since the computational resources would be easily outnumbered. A lightweight Lagrangian reactor solver has been developed for the purpose (Boccelli et al. 2019). Starting from the baseline DSMC solution, our approach marches in time along the precomputed streamlines, calculating chemistry and

multicomponent radial diffusion for metals and free electrons. By doing so, we wish to refine the link existing between the dissipation of the ionized products and the decay in time of the radio echoes in relationship to plasma parameters, with application to radio detection networks (Lamy et al. 2011).

Finally, radiation may be important in the energy balance, even at high altitudes where the gas is considered usually as optically thin: in the shock layer, where it could lead to photoionization (Dias, Scoggins & Magin 2018); in the trail through radiative recombination (Plane et al. 2015). Therefore, its role deserves further investigation.

ACKNOWLEDGEMENTS

The authors acknowledge Stefano Boccelli (Politecnico di Milano) and Bruno Dias (von Karman Institute for Fluid Dynamics) for the fruitful discussion on the topic and the numerous suggestions to improve the quality of the manuscript. We are also grateful to the reviewer for all the comments that considerably helped to improve the manuscript. The research of FB was funded by a PhD grant of the Research Foundation Flanders (FWO).

REFERENCES

Alexander C. M. O., 2001, Meteorit. Planet. Sci., 36, 255
Anderson J. D., 2000, Hypersonic and High Temperature Gas Dynamics, AIAA, Reston, VA
André P. et al., 2010, Eur. Phys. J. D, 57, 227
Baggaley W. J., 1980, in Halliday I., McIntosh B. A., eds, Proc. IAU Symp., 90, 85, IAU, Paris, France
Baggaley W. J., 2002, in Murad E., Williams I. P., eds, Radar observations in Meteors in the Earth's Atmosphere. Cambridge Univ. Press, Cambridge, UK
Berezhnoy A. A., Borovička J., 2010, Icarus, 210, 150
Bird G. A., 1994, Molecular Gas Dynamics and the Direct Simulation of Gas Flows. Oxford Univ. Press, Oxford, UK
Bird R. B., Stewart W. E., Lightfoot E. N., 1960, Transport Phenomena. John Wiley & Sons, New York, NY
Boccelli S., Bariselli F., Dias B., Magin T. E., 2019, Plasma Sources Sci. Technol., 28, 065002
Boitnott C. A., Savage H. F., 1971, ApJ, 167, 349
Bonacina C., Comini G., Fasano A., Primicerio M., 1973, Int. J. Heat Mass Transfer, 16, 1825
Borgnakke C., Larsen P. S., 1975, J. Comput. Phys., 18, 405
Boyd I. D., 1997, Phys. Fluids, 9, 3086
Boyd I. D., 1998, Earth Moon Planets, 82, 93
Briggs D. E., 1968, PhD thesis, Univ. Michigan
Bronshten V. A., 1983, Physics of Meteoric Phenomena. D. Reidel Publishing Co, Dordrecht, Holland
Brun R., 2009, Introduction to Reactive Gas Dynamics. Oxford Univ. Press, Oxford, UK
Bukhteev A. M., Bydin Y. F., 1963, Bull. Acad. Sci. USSR, Phys. Ser., 27, 985
Bydin Y. F., Bukhteev A. M., 1960, Sov. Phys. - Tech. Phys., 5, 512
Campbell-Brown M. D., Koschny D., 2004, A&A, 418, 751
Carlson A. B., Hassan H. A., 1992, J. Thermophys. Heat Transfer, 6, 400
Ceplecha Z., Borovička J., Elford W. G., ReVelle D. O., Hawkes R. L., Porubčan V., Šimek M., 1998, Space Sci. Rev., 84, 327
Cercignani C., 1969, Mathematical Methods in Kinetic Theory. Plenum Press, New York, NY
Cuderman J. F., 1972, Phys. Rev. A, 5, 1687
Dias B., Bariselli F., Turchi A., Frezzotti A., Chatelain P., Magin T. E., 2016, in Ketsdever A., Struchtrup H., eds, Proc. 30th Int. Symp. on Rarefied Gas Dynamics, 1786, 160004, AIP Publishing, Melville, NY
Dias B., Scoggins J. B., Magin T. E., 2018, Eur. Planet. Sci. Congr., 12, 495
Dimant Y. S., Oppenheim M. M., 2017a, J. Geophys. Res.: Space Phys., 122, 4669
Dimant Y. S., Oppenheim M. M., 2017b, J. Geophys. Res.: Space Phys., 122, 4697
Drawin H. W., Emard F., 1973, Phys. Lett. A, 43, 333
Dressler R. A., Murad E., 2001, in Dressler R. A., ed., Chemical Dynamics in Extreme Environments, Advanced Series in Physical Chemistry. World Scientific, Singapore
Fedkin A. V., Grossman L., Ghiorso M. S., 2006, Geochim. Cosmochim. Acta, 70, 206
Fegley B., Cameron A. G. W., 1987, Earth Planet. Sci. Lett., 82, 207
Ferziger J. H., Kaper H. G., 1972, Mathematical Theory of Transport Processes in Gases. Elsevier Science Publishing, Amsterdam, Holland
Frezzotti A., 2011, Phys. Fluids, 23, 030609
Friichtenicht J. F., Slattery J. C., Hansen D. O., 1967, Phys. Rev., 163, 75
Gallis M. A., Torczynski J. R., Plimpton S. J., Rader D. J., Koehler T., 2014, in Fan J., ed, Proc. 29th Int. Symp. on Rarefied Gas Dynamics, 1628, 27, AIP Publishing, Melville, NY
Ghatee M. H., Niroomand-Hosseini F., 2007, J. Chem. Phys., 126, 014302
Giovangigli V., 1999, Multicomponent Flow Modeling. Modeling and Simulation in Science, Engineering and Technology. Birkähuser Boston Inc., Boston, MA
Girin O. G., 2017, A&A, 606, A63
Greenhow J. S., Hall J. E., 1960, MNRAS, 121, 183
Hashimoto A., 1983, Geochem. J., 17, 111
Hashimoto A., 1990, Nature, 347, 53
Hocking W. K., Thayaparan T., Jones J., 1997, Geophys. Res. Lett., 24, 2977
Hocking W. K., Fuller B., Vandepeer B., 2001, J. Atmos. Sol.-Terr. Phys., 63, 155
IMO, International Meteor Organization, https://www.imo.net/resources/databases/
Ivanov M. S., Markelov G. N., Gimelshein S. F., Mishina L. V., Krylov A. N., Grechko N. V., 1998, J. Spacecr. Rockets, 35, 16
Janches D., Dyrud L. P., Broadley S. L., Plane J. M. C., 2009, Geophys. Res. Lett., 36
Jones W., 1995, MNRAS, 275, 812
Jones W., 1997, MNRAS, 288, 995
Josyula E., Burt J., 2011, Technical report, Review of Rarefied Gas Effects in Hypersonic Applications. RTO-EN-AVT-194
Kunc J. A., Soon W. H., 1991, J. Chem. Phys., 95, 5738
Lamy H., Ranvier S., Keyser J., Gamby E., Calders S., 2011, in Cooke W. J., Moser D. E., Hardin B. F., Janches D., eds, Proc. Meteoroids Conf., NASA/CP-2011-216469, 351, NASA Marshall Space Flight Center, Huntsville, AL
LeBeau G. J., 1999, Comput. Methods Appl. Mech. Eng., 174, 319
Lee D. I., Bonilla C. F., 1968, Nucl. Eng. Des., 7, 455
Lennon M. A., Bell K. L., Gilbody H. B., Hughes J. G., Kingston A. E., Murray M. J., Smith F. J., 1988, J. Phys. Chem. Ref. Data, 17, 1285
Loehle S., Jenniskens P., Böhrk H., Bauer T., Elsäßer H., Sears D. W., Zolensky M. E., Shaddad M. H., 2017, Meteorit. Planet. Sci., 52, 197
Love S. G., Brownlee D. E., 1991, Icarus, 89, 26
Love S. G., Brownlee D. E., 1993, Science, 262, 550
Manning L. A., 1958, J. Geophys. Res., 63, 181
McGee B. C., Hobbs M. L., Baer M. R., 1998, Technical report, Exponential 6 Parameterization for the JCZ3-EOS, SAND98-1191. Sandia National Labs., Albuquerque, NM
McKinley D. W. R., 1961, Meteor Science and Engineering. McGraw-Hill, New York, NY
McNeil W. J., Lai S. T., Murad E., 1998, J. Geophys. Res.: Atmos., 103, 10899
Menees G., Park C., 1976, Atmos. Environ., 10:7, 535
Moreno-Ibáñez M., Silber E. A., Gritsevich M., Trigo-Rodríguez J. M., 2018, ApJ, 863, 174
Ogasawara Y., Tabaian S. H., Maeda M., 1998, ISIJ Int., 38, 789
Park C., 1993, J. Thermophys. Heat Transfer, 7, 385
Park C., Menees G. P., 1978, J. Geophys. Res.: Oceans, 83, 4029

Park C., Jaffe R. L., Partridge H., 2001, J. Thermophys. Heat Transfer, 15, 76
Picone J. M., Hedin A. E., Drob D. P., Aikin A. C., 2002, J. Geophys. Res.: Space Phys., 107, SIA 15
Plane J. M. C., 1991, Int. Rev. Phys. Chem., 10, 55
Plane J. M. C., Feng W., Dawkins E. C. M., 2015, Chem. Rev., 115, 4497
Popova O. P., 2004, Earth Moon Planets, 95, 303
Popova O. P., Sidneva S. N., Shuvalov V. V., Strelkov A. S., 2000, Earth Moon Planets, 82-83, 109
Rogers L. A., Hill K. A., Hawkes R. L., 2005, Planet. Space Sci., 53, 1341
Schaefer L., Fegley B., 2004, Icarus, 169, 216
Silber E. A., Hocking W. K., Niculescu M. L., Gritsevich M., Silber R. E., 2017, MNRAS, 469, 1869
Silber E. A., Niculescu M. L., Butka P., Silber R. E., 2018a, Atmosphere, 9, 202
Silber E. A., Boslough M., Hocking W. K., Gritsevich M., Whitaker R. W., 2018b, Advances in Space Research, 62, 489
Stefano D. I., Timorot D. L., Totski Y. Y., 1966, High Temp. Thermophys., 4, 131
Stokan E., Campbell-Brown M. D., 2014, MNRAS, 447, 1580
Sugar G., Oppenheim M. M., Dimant Y. S., Close S., 2018, J. Geophys. Res.: Space Phys., 123, 4080
Svehla R. A., 1962, Technical report, Estimated Viscosities and Thermal Conductivities of Gases at High Temperatures, NASA-TR-R-132. NASA Lewis Research Center, Cleveland, OH
Swaminathan-Gopalan K., Stephani K. A., 2015, Proc. 45th AIAA Thermophysics Conf., 2015-3373, AIAA, Reston, VA
Vargaftik N. B., Vinogradov Y. K., Dolgov V. I., Dzis V. G., Stepanenko I. F., Yakimovich Y. K., Yargin V. S., 1991, Int. J. Thermophys., 12, 85
Verniani F., Hawkins G. S., 1964, ApJ, 140, 1590
Vinković D., 2007, Adv. Space Res., 39, 574
Vondrak T., Plane J. M. C., Broadley S., Janches D., 2008, Atmos. Chem. Phys., 8, 7015
Weryk R. J., Brown P. G., 2013, Planet. Space Sci., 81, 32
Yomogida K., Matsui T., 1983, J. Geophys. Res., 88, 9513

APPENDIX A: MATERIAL RESPONSE ALONG THE ENTRY TRAJECTORY

For a rapidly tumbling sphere (Ceplecha et al. 1998), the heat equation reads as

$$\frac{\partial T}{\partial t} = \frac{k}{\rho C_\mathrm{p}} \frac{\partial^2 T}{\partial r^2} + \frac{2k}{\rho C_\mathrm{p}} \frac{1}{r} \frac{\partial T}{\partial r}, \tag{A1}$$

where k, ρ, and C_p respectively represent the conductivity, density, and specific heat of the meteoroid. The heat equation in this form is obtained by applying a transformation into spherical coordinates $T = T(r, \theta, \varphi, t)$, dropping the angular dependences due to the symmetry of the problem.

The liquid–solid transition is dealt through the *equivalent heat capacity method* by Bonacina et al. (1973). Dias et al. (2016) used this technique to assess the thickness of the liquid layer, which can be taken away by the incoming jet. In this method, only one equation is solved for both the condensed phases without the need for tracking the melting front, which is obtained a posteriori. The latent heat of melting, L_m, at the interface is taken into account by assuming a temperature dependence of the heat capacity of the following type:

$$C_\mathrm{p} = \begin{cases} C_\mathrm{p}^\mathrm{S} & \text{if } T \leq T_\mathrm{m} - \Delta T \\ \frac{C_\mathrm{p}^\mathrm{S} + C_\mathrm{p}^\mathrm{L}}{2} + \frac{L_\mathrm{m}}{2\Delta T} & \text{if } T_\mathrm{m} - \Delta T < T < T_\mathrm{m} + \Delta T \\ C_\mathrm{p}^\mathrm{L} & \text{if } T \geq T_\mathrm{m} + \Delta T \end{cases}, \tag{A2}$$

where T_m is the melting temperature, and ΔT defines the range in which the molten layer and solid coexist, typical feature of melting problems in mixed substances.

Equation (A1) is solved with the following boundary condition at the vapour–liquid interface (indicated with subscript 'w'):

$$\frac{\Lambda \rho_\infty V_\infty^3}{8} = k \frac{\partial T}{\partial r}\bigg|_\mathrm{w} + \epsilon \sigma_\mathrm{s} (T_\mathrm{w}^4 - T_\infty^4) + L_\mathrm{e} \frac{\mathrm{d}m}{\mathrm{d}t}, \tag{A3}$$

which represents a surface energy balance where the thermal energy received by the meteoroid (left-hand side term) is balanced by the heat conduction, radiative, and vapourization losses on the right-hand side. In equation (A3), quantity Λ is the heat transfer coefficient, ϵ the emissivity, σ_s the Stefan–Boltzmann constant, and L_e the latent heat of evaporation.

The freestream velocity V_∞ in the boundary condition is updated along the trajectory by decelerating the body according to the ballistic law

$$\frac{\mathrm{d}V_\infty}{\mathrm{d}t} = -\frac{3}{4} \frac{\rho_\infty}{\rho} \frac{\Gamma}{R} V_\infty^2, \tag{A4}$$

where Γ is the free molecular drag coefficient. The evaporation rate is computed through the Knudsen–Langmuir formula (equation 2), which is set different from zero only when the surface temperature is close to or above the melting condition. Finally, the change in altitude with time, $H(t)$, is a function of the angle of the radiant from the zenith, z_R, as follows:

$$\frac{\mathrm{d}H}{\mathrm{d}t} = -V_\infty \cos(z_\mathrm{R}). \tag{A5}$$

This paper has been typeset from a TEX/LATEX file prepared by the author.